A Projection Method for Incompressible Viscous Flow on a Deformable Domain

by

David Paul Trebotich

B.S.M.E. (University of Mississippi) 1989
M.S. (Tulane University) 1992

A dissertation submitted in partial satisfaction of the

requirements for the degree of

Doctor of Philosophy

in

Engineering–Mechanical Engineering

in the

GRADUATE DIVISION

of the

UNIVERSITY of CALIFORNIA, BERKELEY

Committee in charge:

Professor Phillip Colella, Chair
Professor Alexandre J. Chorin
Professor Panayiotis Papadopoulos

1998

The dissertation of David Paul Trebotich is approved:

Phillip Colella, Chair — Date

Alexandre J. Chorin — Date

Panayiotis Papadopoulos — Date

The University of California, Berkeley
Fall, 1998

A Projection Method for Incompressible Viscous Flow on a Deformable Domain



by

David Paul Trebotich

## Abstract

A Projection Method for Incompressible Viscous Flow on a Deformable Domain
by
David Paul Trebotich

Doctor of Philosophy in Mechanical Engineering
University of California, Berkeley

Professor Phillip Colella, Chair

A second-order accurate finite difference method is presented for numerical solution of the incompressible Navier-Stokes equations on a deformable domain. The target problem is flow in a flexible tube. Fluid motion is forced by movement of the solid wall which requires special treatment of boundary conditions at inflow and outflow. The problem is formulated in terms of a moving, body-fitted coordinate system in $(r, z)$. Mapped coordinates are used to smoothly transform in both time and space the moving domain onto a logically rectangular domain which is fixed in time. The velocity field is split into vortical and potential components. The splitting allows the incompressibility constraint to be enforced in the vortical part and the time-dependent boundary conditions to be carried in the potential component.

The discretization method is based on a new predictor-corrector time discretization which generalizes the Bell-Colella-Glaz method for incompressible flow. Advection terms are obtained by an explicit, second-order Godunov scheme. A MAC projection ensures proper treatment of the pressure and enforcement of the constraint in the advection step. Crank-Nicolson discretization is used to obtain the viscous terms which contain higher-order boundary conditions. Pressure and divergence-free velocity are computed by the application of a Hodge projection. The algorithm is second-order accurate in space and time for a range of laminar flows and domain motions.

---

Committee Chair

# Contents

# List of Figures

# List of Tables

Acknowledgments

The author expresses tremendous gratitude to his thesis advisor, Phil Colella. The successful completion of this thesis is due in large part to Phil. His patience, endurance and expertise are greatly appreciated. The author thanks Alexandre Chorin for his comments and suggestions which have made this thesis much richer, and for his pioneering and continuing work in CFD which led the author into the field. Thanks to Panos Papadopoulos for his keen insight during the course of this project, especially in the areas of finite element methods and continuum mechanics. The author is also indebted to his colleagues in the CFD group and their many helpful conversations and technical assistance. Finally, thanks to friends and family who have supported the author throughout his graduate tenure. *SDG.*

The following sources of funding are acknowledged:

- "Adaptive Numerical Methods for Partial Differential Equations," US Department of Energy Mathematical, Computing, and Information Sciences Division, Grant DE-FG03-94ER25205.
- "Computational Fluid Dynamics and Combustion Dynamics," US Department of Energy High-Performance Computing and Communications Grand Challenge Program, Grant DE-FG03-92ER25140.
- "National Science Foundation Graduate Fellowship Program," National Science Foundation.

# Chapter 1

# Introduction

This thesis presents a numerical model of incompressible viscous flow on a deformable domain. The introductory chapter discusses the evolution of numerical methods that have led to the development of the method. Finite difference models for problems with irregular geometries are briefly described, and then followed by models of problems with deformable domains. Comparison to finite element methods is made, motivating the algorithm.

## 1.1 Numerical Methods

In numerical models of multidimensional problems in fluid dynamics, the frame of reference of the grid in relation to the fluid must be chosen [29]. Classically, the Lagrangian description of a continuum depicts a frame that moves with the continuum. This has led to the development of the finite element method for modeling problems primarily in solid mechanics. For a fluid, however, there is no distinguishable reference configuration for the continuum comparable to the reference configuration for a solid. The frame of reference can be chosen for numerical convenience to depict the motion of a fluid on a fixed domain.

### 1.1.1 Finite Difference Methods

Finite difference methods (FDM's) have been used to model fluid mechanics problems for the last half century. They are a natural choice for the Eulerian description of fluids

as they employ a fixed grid and allow the fluid to flow without a grid to follow it. FDM's are conceptually simple to implement: derivatives in the differential equations are replaced by finite difference approximations. FDM's are not limited to modeling only problems with rectangular geometries. Techniques have been employed to extend the use of FDM's to problems with irregular geometries. Efforts have been made in the area of deformable domains as well. Greater accuracy is now achieved using adaptive techniques in the more interesting regions of a flow domain.

### Projection Methods

Chorin [13] developed the projection method for solving the incompressible Navier-Stokes equations. The procedure is based on the Hodge decomposition of any vector field into a divergence-free part and a gradient of a scalar field. It is a fractional step method which first predicts an intermediate velocity that does not necessarily satisfy the incompressibility constraint, then corrects this velocity so that it satisfies the constraint.

The starting point for the present work is the second-order projection method of Bell, Colella and Glaz (BCG) [4]. They introduced a higher-order Godunov method to obtain a more robust convective derivative, especially in the presence of underresolved gradients, as well as a predictor-corrector method that approximates Crank-Nicolson. Bell, Colella and Howell [5] improved the BCG method by adding a MAC-type projection to the predictor in order to eliminate an instability for CFL numbers greater than 0.5. Bell and Marcus [7] extended the projection to variable density flows by incorporating a discrete density-weighted vector inner product into the definition of the discrete projection operator. Almgren, Bell and Szymczak [1] computed a velocity field which is not discretely divergence-free because their projection only approximately enforces the incompressibility constraint. Lai [39] also employed an approximate projection method with a filter for the persistent non-physical oscillatory modes of reacting flow in the zero Mach number limit.

### Irregular Domains

In the finite difference community, there are several approaches to fixed, irregular domains. First, in a mapped grid approach [6, 17], a mapping transforms a fixed space of logically rectangular cells into a grid of arbitrary quadrilateral or hexahedral cells. The BCG algorithm was extended to mapped grids by Bell et al. [8]. Colella and Johansen did further work with an approximate projection on mapped grids for variable density [37].

In the Cartesian grid method [2], an irregular boundary is embedded in a Cartesian mesh. At boundaries, where irregular cells result, a volume of fluid approach [33] is employed in order to conserve mass. At interior points, the method facilitates use of higher-order finite difference discretization procedures. Two dimensional problems can be extended to three dimensions in an obvious manner.

Overset grids and multiblock methods are also approaches to irregular domains. Overset grids are simply mapped grids that are allowed to overlap. Multiblock methods have been used to treat very complex configurations, particularly in aerodynamics applications [55, 59]. In this approach there are blocks of separately generated meshes which must be patched at block interfaces. An alternative to the structured grid methods for complicated irregular geometries is unstructured grids. In an unstructured mesh, the domain is subdivided into tetrahedra. In both cases, grid generation is a nontrivial issue.

### Deformable Domains

For the case of a deformable domain as in the example of a fluid-solid interaction, the grid is not only irregular but also deformable. Arbitrary Lagrangian-Eulerian (ALE) schemes were originally developed in the finite difference format to handle such scenarios [50, 58]. The early work of Hirt, Amsden and Cook [32] is noteworthy in that it is applicable to arbitrary finite difference meshes and treats flows of all speeds.

Much success in the area of FDM's and moving boundaries has been achieved in the area of cardiac fluid dynamics. Peskin initially extended Chorin's incompressible Navier-

Stokes method to model flow patterns around heart valves using an immersed boundary method [51]. In a later model, a coupled fluid-fiber system is solved using a FDM on a fixed grid for the fluid while valve and muscle fiber points move freely about the lattice [52]. A smooth interpolation scheme accounts for the coupled motion. Fluid exists on both sides of the boundary in these models.

More recently, Cortez used a method based on magnetization variables where the effect of boundary forces on an incompressible inviscid fluid is transmitted via vortex dipoles [19]. This work applies to potential flow where all the flow dynamics are occurring at the boundary. LeVeque developed a second-order accurate interface tracking method for steady Stokes flow with time-dependent forcing for moving interfaces on a uniform Cartesian grid [40]. Also, Johansen and Colella extended the Cartesian grid embedded boundary method to time-dependent domains as they apply to crystal growth [36].

The present work in regard to deformable domains in FDM's is based on the standard of moving, mapped grids [6]. In moving quadrilateral grids, a fixed rectangular domain is mapped into a moving frame which depicts the real motion of the problem. Discrete temporal derivatives must be performed in the fixed space because of the relative motion of the physical frame. Also, the typical accuracy studies reside on the fixed, rectangular space. Bell et al. [6] proposed moving quadrilateral grids for unsteady gas dynamics with the addition of adaptive mesh refinement (AMR). Colella's development of multidimensional unsplit, upwind methods for hyperbolic conservation laws also included extension to time-dependent problems using quadrilateral meshes [17].

### 1.1.2 Finite Element Methods

Finite element methods (FEM's) are also used to model time-dependent hyperbolic problems like fluid flows [26]. They have been extensively used where irregular moving boundaries are present [23, 44]. An advantage of FEM's is that they are amenable to inhomogeneous boundary conditions. However, the line between FEM's and FDM's becomes

blurred when attempting to use a finite element spatial discretization with a standard time-stepping procedure to model a hyperbolic problem (see Morton [46] for a comparison between the two methodologies).

FEM's use an integral-type approach to develop a numerical equivalent of the flow equations. The most general approach is the method of weighted residuals. This technique forms an integral equation by multiplication of the flow equations by a weighting function and then integration over a prescribed interval [54]. Several methods have been developed from this approach. The classic method within this framework is the pure Galerkin method.

FEM's are spatial discretizations; therefore, the Galerkin method must be coupled with standard time-stepping algorithms (Crank-Nicolson, backward Euler, Lax-Wendroff or Runge-Kutta, for example) to address time-dependent advection problems. Donea notes several disadvantages to this coupled approach: it suffers from a rapid fall off in accuracy as the time step is increased, and it has a reduced range of stability as compared to a corresponding FDM [24].

Deficiencies in the coupling of the classical Galerkin method with standard integrators for advection dominated problems motivated the development of generalized Galerkin methods [22, 24, 47]. In the generalized approach, the weights are integrated differently than the velocity and pressure. Also, most of these methods more properly account for the link between space and time via the direct or indirect use of characteristics. The Petrov-Galerkin method is an early upwind FEM used to model the one-dimensional linear wave equation where special weighting functions are used [30, 48]. Streamline upwinding has been added to Petrov-Galerkin to modify the weighting function [11]. This yields a consistent formulation without the familiar spurious wiggles of the pure method [22]. Taylor-Galerkin methods are different in that the discretization in time is addressed before the spatial discretization in an attempt to achieve greater accuracy [21]. They are based on Taylor series expansions in the time step and do not account for characteristic behavior. Least-squares Galerkin methods add least-squares forms of residuals to the standard Galerkin approach in order to improve

stability and maintain accuracy. They are simple to implement like Taylor methods and unconditionally stable like characteristic-based methods, but lose accuracy rapidly when the CFL number exceeds unity [24, 34]. Stabilized space-time FEM's have been introduced to overcome limitations in the classical Galerkin approach when modeling the incompressible Navier-Stokes equations by FEM's [26, 27, 38, 34]. There is no confusion with FDM's in these methods as time is discretized by a finite element approximation.

In the area of deformable domains, FEM discretizations lend themselves to implementation in ALE methods because of the fitting of mixed grids, fluid and solid for example [20]. These methods were developed in response to the need for versatile treatment of transient fluid-structure systems [9, 23, 35]. ALE finite element formulations have incorporated recent advances in FEM's to model incompressible viscous flow on moving domains [44].

### Thesis Purpose and Overview

The purpose of this thesis is to present a second-order accurate finite difference method to solve the incompressible Navier-Stokes equations on deformable domains. There are two primary issues to address: (1) inhomogeneous boundary conditions and deformable domains, and (2) a time-dependent incompressibility constraint. The first issue is addressed by a split-velocity formulation [15, 16, 18, 31] on moving, mapped grids [6]. This formulation is analogous to a vortex method [15, 57] where the velocity is defined such that there is no flux across a boundary for the divergence-free component. Inhomogeneous normal boundary conditions are automatically satisfied at all times through solution to the potential flow problem. Also, the need to evolve the divergence-free component of velocity remains and requires enforcement of a time-dependent incompressibility constraint and extraction of the pressure.

The second issue is addressed by a new time discretization which generalizes the BCG method. The incompressibility constraint is always satisfied because the discretization requires application of only a succession of fixed time operators rather than solution to

problems resulting from differentiation of the constraint with respect to time. Second-order accuracy of the method is shown analytically and corroborated by the computational results. The issues addressed here are closely related to those that arise in discretization of differential/algebraic equations. Petzold addressed systems of differential/algebraic equations which have the form of the model problem discussed in this thesis [53]. Plasticity with the yield condition is an example of a time-dependent constrained system where accuracy of models has been studied [25, 56].

This introduction has been a discussion of the background and motivation of a projection method for unsteady, incompressible viscous flows on deformable domains. The remainder of this thesis is devoted to mathematical and numerical development of the method. In chapter two, all the mathematical issues needed to develop an analytical model for the target problem of flow in a flexible tube are addressed: the Hodge projection, moving, mapped grids and a split-velocity formulation. The new time discretization based on the BCG method is then discussed in the context of a model problem in chapter three. The complete algorithm along with numerical tools is also described in that chapter. Finally, chapter four is a presentation and discussion of the results obtained by the algorithm. Direction for future work is also recommended.

# Chapter 2

# Equations of Motion

This chapter discusses the issues involved with modeling the equations of motion for a time-dependent constrained system as it applies to incompressible viscous flow on a deformable domain. It begins with a presentation of mathematical concepts needed to describe the time evolution of such a system while enforcing the incompressibility constraint. The restricted example of incompressible viscous flow in a rigid box is put forward as a reference for the more complicated problem of flow in a time-dependent domain. Deformable boundaries are then discussed in the context of flow in a flexible tube. The necessary mathematical tools to deal with a deformable domain are presented and applied within the framework of a constraint formulation. The importance of the special case of potential flow with time-dependent boundaries is noted as well. Problems with inhomogeneous boundary conditions are discussed in detail, and a remedy is proposed.

## 2.1 Hodge Decomposition

The focus of the mathematical model for an unsteady incompressible flow on any domain is the derivation of an evolution equation. This is no trivial task as the pressure has to be properly accounted for while enforcing the incompressibility constraint. The Hodge decomposition is a means of achieving this task.

### Hodge Decomposition

The Hodge decomposition [14] (derivable from the Helmholtz representation theorem in continuum mechanics [3, 28]) is a splitting of any smooth vector field on a simply connected domain into two orthogonal components: a divergence-free part, and a gradient of a scalar field. If $\mathbf{w} = \mathbf{w}(\mathbf{x})$ is vector field defined on a simply connected domain, $\Omega$, then $\mathbf{w}$ can be orthogonally decomposed as follows:

$$\mathbf{w} = \mathbf{w}_d + \nabla\varphi \tag{2.1}$$

such that

$$\int_\Omega (\mathbf{w}_d \cdot \nabla\varphi) d\mathbf{x} = 0. \tag{2.2}$$

The divergence-free part, $\mathbf{w}_d$, satisfies $\nabla \cdot \mathbf{w}_d = 0$ with $\mathbf{w}_d \cdot \mathbf{n} = 0$ on the boundary, $\partial\Omega$. The scalar field, $\varphi$, is defined by the Poisson's equation which it satisfies, $\Delta\varphi = \nabla \cdot \mathbf{w}$ on $\Omega$, with boundary conditions $\frac{\partial\varphi}{\partial\mathbf{n}} = \mathbf{w} \cdot \mathbf{n}$ on $\partial\Omega$.

### Hodge Projection

The Hodge decomposition motivates the definition of a projection operator (see Chorin [12, 13, 14]). Let *div* be the divergence operator, $div(\mathbf{w}) = \frac{\partial w_i}{\partial x_i}$, and *grad* be the gradient operator, $grad_j(\mathbf{w}) = \frac{\partial \mathbf{w}}{\partial x_j}$. The relationship between normal boundary conditions and the divergence operator is shown in the divergence theorem:

$$\int_\Omega (\nabla \cdot \mathbf{w}) d\mathbf{x} = \int_{\partial\Omega} (\mathbf{w} \cdot \mathbf{n}) ds. \tag{2.3}$$

The divergence theorem requires $\mathbf{w}$ to be sufficiently smooth and the surface normal, $\mathbf{n}$, to be uniquely defined at all points on $\partial\Omega$.

Define $\mathbf{P}$ to be the projection operator which extracts the divergence-free part of a vector: $\mathbf{P}(\mathbf{w}) = \mathbf{w}_d$. The gradient of the potential can be written in projection form as $grad(\varphi) = (\mathbf{I} - \mathbf{P})\mathbf{w}$. The projection is defined as

$$\mathbf{P} = (\mathbf{I} - grad(div\, grad)^{-1} div) \tag{2.4}$$

where $\mathbf{I}$ is an identity operator. Boundary conditions for the projection are specified in *div* and *grad*. Some properties of the projection operator are symmetry, $\mathbf{P} = \mathbf{P}^T$, and idempotence, $\mathbf{P}^2 = \mathbf{P}$.

### 2.1.1 Incompressible Flow

The equation of motion for any continuum as derived from momentum principles (see Naghdi [49]) is

$$\rho \mathbf{u}_t = \nabla \cdot \boldsymbol{\tau} + \rho \mathbf{b} \tag{2.5}$$

where $\mathbf{u}$ is the continuum velocity, $\boldsymbol{\tau}$ is the symmetric stress tensor, $\rho$ is density and $\mathbf{b}$ represents body forces. Consider the special case of a Newtonian fluid where the stress tensor is linearly dependent on the rate of deformation, $\frac{\partial \mathbf{u}}{\partial \mathbf{x}}$, with coefficients dependent on the density, $\rho$. It can be shown through invariance requirements that the stress tensor is comprised of invariant isotropic tensor functions [49]:

$$\boldsymbol{\tau} = -p\mathbf{I} + \lambda \nabla \cdot \mathbf{u} + 2\mu \nabla \mathbf{u} \tag{2.6}$$

where $\lambda$ and $\mu$ are viscosity coefficients and $p$ is a density-dependent scalar which acts normal to the surface of the fluid. This is the Navier-Poisson Law for a Newtonian fluid [43]. Substitution of (2.6) into (2.5) yields the Navier-Stokes equations:

$$\mathbf{u}_t + \nabla \cdot (\mathbf{u} \otimes \mathbf{u}) = -\nabla p + \nu \Delta \mathbf{u} \tag{2.7}$$

where body forces have been neglected. To solve the Navier-Stokes equations (2.9), an additional equation for conservation of mass is needed:

$$\rho_t + \rho \nabla \cdot \mathbf{u} = 0. \tag{2.8}$$

For the problems of interest in this thesis, it is assumed that density is constant. Therefore, the equations of motion for an incompressible, linear viscous fluid, also known as the incompressible Navier-Stokes equations, are the Navier-Stokes equations

$$\mathbf{u}_t + \mathbf{u} \cdot \nabla \mathbf{u} = -\nabla p + \nu \Delta \mathbf{u} \tag{2.9}$$

plus the incompressibility constraint

$$\nabla \cdot \mathbf{u} = 0. \tag{2.10}$$

**Flow in a Box**

Consider flow in a box with rigid walls ($\mathbf{u} \cdot \mathbf{n} = 0$ on $\partial\Omega$) where there is initial vorticity (see Figure 2.1). In order to completely solve the system of equations (2.9) and (2.10), boundary conditions and a relation for the pressure must be obtained given an equation of motion. It is first noted that the incompressibility constraint (2.10) is applied to the velocity and the momentum equation (2.9) depends on the acceleration. For a fixed domain, the constraint, as well as boundary conditions, can be differentiated:

$$\begin{aligned} (\nabla \cdot \mathbf{u})_t = 0 \quad &\longrightarrow \quad \nabla \cdot \mathbf{u}_t = 0 \\ (\mathbf{u} \cdot \mathbf{n})_t = 0 \quad &\longrightarrow \quad \mathbf{u}_t \cdot \mathbf{n} = 0. \end{aligned} \tag{2.11}$$

(The constraint can always be differentiated due to commutativity of temporal and spatial operators which are referred to the same basis.) The differentiated constraint combined with the divergence of the Navier-Stokes equations (2.9) yields a relation for pressure:

$$\Delta p = \nabla \cdot (-\mathbf{u} \cdot \nabla \mathbf{u} + \nu \Delta \mathbf{u}). \tag{2.12}$$

where the convective derivative has been simplified using conservation of mass (2.10). The pressure boundary condition follows from the normal component of the Navier-Stokes equations (2.9) using the differentiated boundary condition in (2.11):

$$\frac{\partial p}{\partial \mathbf{n}} = \mathbf{n} \cdot (-\mathbf{u} \cdot \nabla \mathbf{u} + \nu \Delta \mathbf{u}). \tag{2.13}$$

The problem can be reformulated by applying the Hodge projection directly to the Navier-Stokes equations (2.9) and incorporating the incompressibility constraint (2.10):

$$\begin{aligned} \mathbf{u}_t &= \mathbf{P}(-\mathbf{u} \cdot \nabla \mathbf{u} + \nu \Delta \mathbf{u}) \\ \nabla p &= (\mathbf{I} - \mathbf{P})(-\mathbf{u} \cdot \nabla \mathbf{u} + \nu \Delta \mathbf{u}). \end{aligned} \tag{2.14}$$

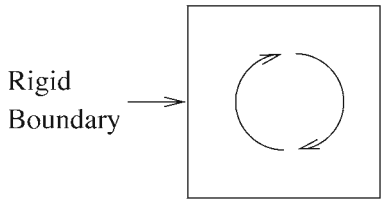


**Figure 2.1:** Flow in a rigid box.

**Remarks**

The projection formulation provides a framework to solve the incompressible Navier-Stokes equations (2.9) and (2.10) on a fixed domain. Normal boundary conditions are dealt with in a straightforward manner by differentiation (2.11) and application through the divergence theorem for the acceleration (2.3). The projection formulation also displays the character of the pressure gradient, $\nabla p$, as the piece which is stripped away from the right-hand side when incompressibly constraining the fluid by application of the projection operator. Finally, the projection formulation reduces the differential equations (2.9) and incompressibility constraint (2.10) to an initial value problem (IVP). Given initial conditions that satisfy the constraint, this is a well-posed problem.

## 2.2 Deformable Boundaries

The projection method provides a framework in which to deal with viscous flow in a rigid box. What if the geometry is irregular? Even more, what if the boundaries of a flow problem are not fixed, but, rather, time-dependent? This section presents the physical problem of flow in a flexible tube. Mathematical tools needed to obtain proper equations of motion are first described. Then the inviscid case of potential flow past a deformable boundary is discussed with particular attention given to boundary conditions.

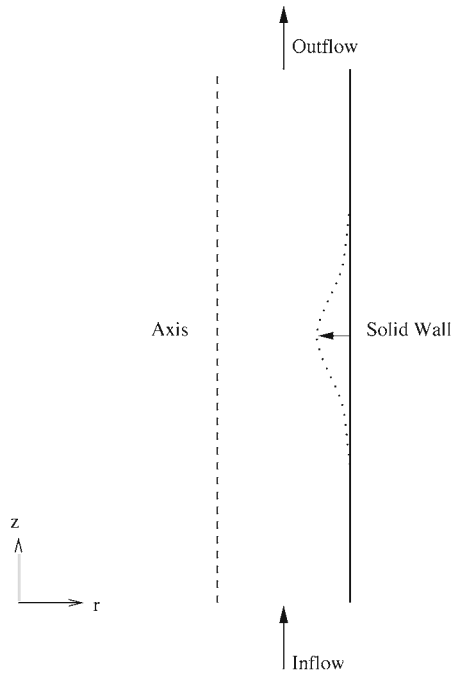


**Figure 2.2:** Flow through a flexible tube.

### 2.2.1 Flow in a Flexible Tube

Consider viscous flow through a straight, flexible tube (see Figure 2.2). The dashed left boundary of the figure is the centerline, or axis of symmetry, of the tube where $r = 0$. It does not bend, thus, making this a two-dimensional, axisymmetric flow. There is flow into the tube at the bottom boundary. At this inlet the classic Poiseuille velocity profile for viscous flow in pipes is prescribed. The wall of the tube is the right boundary, $r = R(z, t)$. This infinitely thin solid wall boundary is allowed to move in the middle section of the tube with a prescribed velocity. The inlet and outlet remain fixed. It is of interest in this chapter of the thesis to derive equations of motion which mathematically model the physics of the fluid flow in response to the prescribed conditions.

### Calculus Preliminaries

Define a continuous mapping from an abstract fixed coordinate system, $\boldsymbol{\xi} = (\xi, \eta)$, to real axisymmetric coordinates which are time-dependent, $\mathbf{x}(t) = (r(t), z(t))$:

$$\mathbf{x} = \boldsymbol{\chi}(\boldsymbol{\xi}, t). \tag{2.15}$$

A transformation matrix, $\mathbf{F}$, and its inverse, $\mathbf{F}^{-1}$, can be defined from this mapping:

$$\mathbf{F} = \nabla_{\xi}\mathbf{x} = \begin{bmatrix} \mathrm{r}_{\xi} & \mathrm{r}_{\eta} \\ \mathrm{z}_{\xi} & \mathrm{z}_{\eta} \end{bmatrix} \quad \text{and} \quad \mathbf{F}^{-1} = gJ^{-1} \begin{bmatrix} \mathrm{z}_{\eta} & -\mathrm{r}_{\eta} \\ -\mathrm{z}_{\xi} & \mathrm{r}_{\xi} \end{bmatrix} \tag{2.16}$$

where $J$ is the non-zero Jacobian of transformation

$$J = det\mathbf{F} = g(r_{\xi}z_{\eta} - r_{\eta}z_{\xi}) \tag{2.17}$$

and $g = 2\pi r$ is a factor referred to as the volume metric. The inverse transformation matrix, $\mathbf{F}^{-1}$, is a significant quantity. It must be derived from the transformation matrix in three dimensions in order to account for proper volume weighting.

The mapping (2.15) is applied to dependent variables of the Navier-Stokes equations as follows:

$$\mathbf{u}(\mathbf{x}, t) = \mathbf{u}(\boldsymbol{\chi}(\xi, t), t). \tag{2.18}$$

The chain rule is used to compute the relationship between the derivative $\mathbf{u}_t|_{\xi}$ with $\boldsymbol{\xi}$ held fixed and the derivative $\mathbf{u}_t|_x$ with $\mathbf{x}$ held fixed:

$$\mathbf{u}_t|_x = \mathbf{u}_t|_{\xi} - \frac{\partial \mathbf{u}}{\partial \mathbf{x}} \frac{\partial \mathbf{x}}{\partial t} = \mathbf{u}_t|_{\xi} - \mathbf{s} \cdot \nabla \mathbf{u} \tag{2.19}$$

where $\mathbf{s} = \frac{\partial \mathbf{x}}{\partial t}$ is the relative velocity of the coordinate system $\mathbf{x}$. Spatial operators in mapped coordinates are represented by direct application of the chain rule to the relative derivatives. Indicial notation in conjunction with the summation convention [49] is best suited for obtaining the correct direct representation as seen, for example, in the divergence:

$$\nabla_x \cdot \mathbf{u} = \frac{\partial u_i}{\partial x_i} = \frac{\partial u_i}{\partial \xi_j} \frac{\partial \xi_j}{\partial x_i} = \frac{\partial u_i}{\partial \xi_j} \mathbf{F}^{-1}_{ji} = J^{-1} \nabla_{\xi} \cdot J\mathbf{F}^{-1}\mathbf{u}. \tag{2.20}$$

The gradient is expressed in a similar manner:

$$(\nabla_x p)_{i,j} = \frac{\partial p_i}{\partial x_j} = \frac{\partial p_i}{\partial \xi_l}\frac{\partial \xi_l}{\partial x_j} = \frac{\partial p_i}{\partial \xi_l}\mathbf{F}^{-1}_{lj} = (\mathbf{F}^{-T}\nabla_\xi p)_{i,j}. \tag{2.21}$$

The Laplacian operator, $\Delta$, is defined as the divergence of the gradient:

$$\Delta\phi = \nabla_x \cdot \nabla_x \phi = J^{-1}\nabla_\xi \cdot J\mathbf{F}^{-1}\mathbf{F}^{-T}\nabla_\xi \phi. \tag{2.22}$$

**Transformed Equations of Motion**

Application of the mapped coordinate definitions to (2.9) and (2.10) yields the incompressible Navier-Stokes equations in generalized mapped coordinates:

$$\begin{aligned} \mathbf{u}_t|_\xi + J^{-1}(\bar{\mathbf{u}} - \bar{\mathbf{s}}) \cdot \nabla_\xi \mathbf{u} &= -\mathbf{F}^{-T}\nabla_\xi p + \nu J^{-1}\nabla_\xi \cdot (J\mathbf{F}^{-1}\mathbf{F}^{-T}\nabla_\xi \mathbf{u}) \\ \nabla_\xi \cdot (J\mathbf{F}^{-1}\mathbf{u}) &= 0 \end{aligned} \tag{2.23}$$

where velocities are transformed to the $\boldsymbol{\xi}$ basis as

$$\bar{\mathbf{u}} = J\mathbf{F}^{-1}\mathbf{u}. \tag{2.24}$$

**Boundary Conditions**

The kinematic boundary conditions are as follows (refer to Figure 2.2 for geometry):

(1) axis of symmetry (no flow across centerline of tube)

$$\mathbf{u} \cdot \mathbf{n} = 0, \tag{2.25}$$

(2) solid wall (prescribed boundary velocity)

$$\mathbf{u} = \mathbf{u}_b, \tag{2.26}$$

(3) inflow (prescribed Poiseuille flow)

$$\begin{aligned} u &= 0 \\ v(r) &= 2(1 - r^2), \end{aligned} \tag{2.27}$$

(4) outflow

$$\frac{\partial \mathbf{u}}{\partial z} = 0. \tag{2.28}$$

Also, initial conditions must be prescribed, or known from restrictions of the physical model, for the problem to be a well-posed IVP.

### 2.2.2 Potential Flow

Consider the Euler momentum equation for an incompressible inviscid fluid:

$$\mathbf{u}_t|_x + \mathbf{u} \cdot \nabla \mathbf{u} = -\nabla p. \tag{2.29}$$

If the velocity is irrotational, then it can be written as a gradient of a scalar potential, $\mathbf{u} = \nabla \Phi$. Substituting the potential velocity relation into (2.29) and transforming the coordinates yields Bernoulli's equation:

$$\left.\frac{\partial \phi}{\partial t}\right|_{\xi} - \bar{\mathbf{s}} \cdot \nabla_{\xi} \phi + \frac{|\mathbf{u}|^2}{2} + p = constant. \tag{2.30}$$

The constant of integration is defined as the Bernoulli pressure:

$$\pi = \left.\frac{\partial \phi}{\partial t}\right|_{\xi} - \bar{\mathbf{s}} \cdot \nabla_{\xi} \phi + \frac{|\mathbf{u}|^2}{2} + p. \tag{2.31}$$

Potential flow is the steady irrotational flow of an incompressible inviscid fluid. A potential function, $\Phi$, can be defined such that the potential velocity can be written as a pure gradient, $\mathbf{u}_p = \nabla \Phi$. Potential flow is a boundary value problem (BVP). Given normal boundary conditions on the velocity, the solution is obtained at any time by solving the following Poisson equation:

$$\Delta \Phi = 0. \tag{2.32}$$

The temporal dependence of this problem is found in the boundary conditions which are applied in the fluxes at their respective boundaries as defined by the divergence theorem:

$$\int_{\mathcal{V}} (\nabla \cdot \mathbf{u}) d\mathcal{V} = \int_{\mathcal{A}} (\mathbf{u} \cdot \mathbf{n}) d\mathcal{A}. \tag{2.33}$$

The divergence theorem demonstrates that the potential component of a flow is defined by normal boundary conditions [15, 57].

The normal boundary conditions for potential flow in a flexible tube are as follows (see Figure 2.2 for geometry):

(1) axis of symmetry (no-flow)

$$\mathbf{u}_p \cdot \mathbf{n} = 0, \tag{2.34}$$

(2) solid wall (prescribed boundary motion)

$$\mathbf{u}_p \cdot \mathbf{n} = \mathbf{u}_b \cdot \mathbf{n}, \tag{2.35}$$

(3) inflow (constant plug flow)

$$\mathbf{u}_p \cdot \mathbf{n} = v_{in}, \tag{2.36}$$

(4) outflow (conservation of mass, 1D flow)

$$\mathbf{u}_p \cdot \mathbf{n} = v_{out} \tag{2.37}$$

where $v_{out}$ is calculated from conservation of mass for flow in a flexible tube with fixed inlet and outlet:

$$\int_0^{R_{out}} 2\pi r(\mathbf{u}_p \cdot \mathbf{n})dr + \int_0^{R_{in}} 2\pi r(\mathbf{u}_p \cdot \mathbf{n})dr + \int_0^{L_{wall}} 2\pi R(l)(\mathbf{u}_p \cdot \mathbf{n})dl = 0. \tag{2.38}$$

## 2.3 Problems with the Constraint Formulation

For viscous flow on a fixed domain (flow in a rigid box, for example), the constraint formulation yields a well-posed IVP via differentiation of the incompressibility constraint and boundary conditions with respect to time. For deformable domains, this formulation runs into problems. Boundary conditions cannot be temporally differentiated as in the fixed case (2.11) without leading to an inhomogeneous term. Furthermore, the solid wall

boundary condition is inhomogeneous. Also, the outflow boundary condition is an issue because of the viscous flow, in general, and because it depends on the time-dependent solid wall condition. More fundamentally, however, the divergence constraint is both time-dependent and inhomogeneous.

### 2.3.1 Inhomogeneous Boundary Conditions

In accordance with the definition of the transformation (2.15) and how it is applied to the time-dependent domain (2.19), it is proper to perform time-differentiation of quantities on a deformable domain holding the mapped coordinate, $\boldsymbol{\xi}$, fixed–not $\mathbf{x}$–since it is the computational space which is not time-dependent. Also, the relative motion term which appears in (2.19) will have to be accounted for in either case. In mapped coordinates, the velocity boundary condition at the wall, for example, is $(J\mathbf{F}^{-1}\mathbf{u})|_{wall} = 0$, where the inhomogeneous part is omitted for the sake of seeing only the inhomogeneous contribution of the time-dependent domain. This condition is differentiated with respect to time in fixed $\boldsymbol{\xi}$ coordinates resulting in an inhomogeneous boundary condition for the acceleration:

$$\mathbf{n}_\xi \cdot \left.\frac{\partial \mathbf{u}}{\partial t}\right|_\xi = \left(\mathbf{n}_\xi \cdot \frac{\partial \mathbf{s}}{\partial \eta}\right) \frac{1}{J} (\mathbf{n}_\eta \cdot \mathbf{u}) \tag{2.39}$$

where the following relations have been used for the derivative of the Jacobian and the inverse transformation, respectively:

$$\begin{aligned} \left.\frac{\partial J}{\partial t}\right|_\xi &= J \nabla \cdot \mathbf{s} \\ \left.\frac{\partial \mathbf{F}^{-1}_{ij}}{\partial t}\right|_\xi &= \mathbf{F}^{-1}_{il} s_{l,m} \mathbf{F}^{-1}_{mj}. \end{aligned} \tag{2.40}$$

(Indicial notation is employed to extract the component of the inverse transformation, $\mathbf{F}^{-1}$, which corresponds to the normal at the boundary of choice, the solid wall in this case.) The boundary condition for acceleration can be transformed to the real coordinate system through the relative convective derivative:

$$\mathbf{n} \cdot \left.\frac{\partial \mathbf{u}}{\partial t}\right|_x = \left(\mathbf{n}_\xi \cdot \frac{\partial \mathbf{s}}{\partial \eta}\right) \frac{1}{J} (\mathbf{n}_\eta \cdot \mathbf{u}) - \mathbf{n}_\xi \cdot (\mathbf{s} \cdot \nabla \mathbf{u}). \tag{2.41}$$

This expression is complicated by the appearance of the velocity itself, as well as the relative convective derivative. It is again noted that added terms would result from including the derivative of the inhomogeneous part of the velocity boundary condition at the solid wall.

### 2.3.2 Inhomogeneous Constraint

For fixed domains, the incompressibility constraint can be differentiated with respect to time (2.11) leaving a homogeneous constraint for acceleration. Though this differentiation also holds true for time-dependent domains, there is an inhomogeneity in the divergence constraint created by differentiation of metric terms and applied through the divergence theorem (2.3) in fluxes at boundaries. The right-hand side of the constraint is, thus, no longer zero. Another term is added to the right-hand side when the velocity boundary condition itself is inhomogeneous, as is the case at deformable solid walls.

The necessity for proper temporal differentiation in a numerical setting is foreseen at this point. However, in an attempt to correctly differentiate the incompressibility constraint in a temporally fixed coordinate system, the unavoidable differentiation of metric terms appears,

$$\left.\frac{\partial}{\partial t}\right|_{\xi} (\nabla_x \cdot \mathbf{u}) = 0 \longrightarrow \left.\frac{\partial}{\partial t}\right|_{\xi} (\frac{1}{J}\nabla_\xi \cdot J\mathbf{F}^{-1}\mathbf{u}) = 0, \tag{2.42}$$

leading to yet more inhomogeneous terms.

#### Remarks

If the incompressibility constraint is differentiated, time-centering of the constraint (as well as boundary conditions) presents difficulties in the numerical implementation of this problem. Outstanding questions also remain in regard to numerical stability and overall second-order accuracy of a method built on this kind of theory. These issues are sufficient to motivate new formulations for unsteady incompressible flows on deformable domains.

## 2.4 Split-Velocity Formulation

The constraint formulation defines a well-posed IVP for unsteady, incompressible viscous flow on a deformable domain. Analytically, the incompressibility constraint and boundary conditions are well-behaved and known at this point, but numerical implementation is a formidable challenge. The interdependent relationship between boundary conditions and the constraint introduced by the necessity of time-differentiation behooves a decoupling of the two, if possible. There is also the issue of an inhomogeneous kinematic condition at solid walls and the question of what to do at outflow. The Hodge decomposition in conjunction with knowledge of potential flow provides the insight needed to separate the two issues, leading to a new formulation. The first task of the split-velocity (SV) formulation is to alleviate the problem of inhomogeneous and time-dependent velocity boundary conditions for flow through a flexible tube. It is concluded that the solution to problems with boundary conditions in general is to split the velocity field into its divergence-free (vortical) and potential components (see [18, 31]).

### 2.4.1 Split Velocity Field

Introduce a velocity field such that it is comprised of divergence-free and potential components, $\mathbf{u}_d$ and $\mathbf{u}_p$, respectively:

$$\begin{aligned} \mathbf{u} &= \mathbf{u}_d + \mathbf{u}_p \\ \nabla \cdot \mathbf{u}_d &= 0 \\ \mathbf{u}_p &= \nabla \phi. \end{aligned} \tag{2.43}$$

#### Boundary Value Problem

The splitting leads to two important results. First, the potential velocity is given by

$$\mathbf{u}_p = \mathbf{F}^{-T} \nabla_\xi \phi \tag{2.44}$$

and satisfies the well-posed BVP in mapped coordinates for all times

$$\nabla_\xi \cdot (J\mathbf{F}^{-1}\mathbf{F}^{-T}\nabla_\xi \phi) = 0. \tag{2.45}$$

Boundary conditions for the potential flow solution are given in (2.34-2.38).

**Equation of Motion**

The second result of the splitting (2.43) is an equation of motion for the divergence-free component of velocity. Consider the equation of motion (2.9) while holding $\mathbf{x}$ fixed. The temporal derivative of velocity splits simply as

$$\left.\frac{\partial \mathbf{u}}{\partial t}\right|_x = \left.\frac{\partial \mathbf{u}_d}{\partial t}\right|_x + \left.\frac{\partial \mathbf{u}_p}{\partial t}\right|_x. \tag{2.46}$$

The derivative of the potential component is extracted as a pure gradient:

$$\left.\frac{\partial \mathbf{u}_p}{\partial t}\right|_x = \left.\frac{\partial (\nabla_x \phi)}{\partial t}\right|_x = \nabla_x \left( \left.\frac{\partial \phi}{\partial t}\right|_x \right) \tag{2.47}$$

making use of the commutativity of spatial and temporal operators in the same basis. The convective derivative splits in the following manner:

$$\mathbf{u} \cdot \nabla \mathbf{u} = \mathbf{u} \cdot \nabla \mathbf{u}_d + \mathbf{u}_d \cdot \nabla \mathbf{u}_p + \mathbf{u}_p \cdot \nabla \mathbf{u}_p. \tag{2.48}$$

A vector identity can be employed to simplify the purely potential convective derivative:

$$\mathbf{u}_p \cdot \nabla \mathbf{u}_p \equiv \nabla \frac{|\mathbf{u}_p|^2}{2} + \omega \times \mathbf{u}_p \tag{2.49}$$

recalling $\omega = \nabla \times \mathbf{u}_p = 0$. A Bernoulli pressure is then defined to consume all outstanding gradients:

$$\pi \equiv \left.\frac{\partial \phi}{\partial t}\right|_x + \frac{|\mathbf{u}_p|^2}{2} + p = constant. \tag{2.50}$$

The resulting equation of motion for the divergence-free velocity field, $u_d$, in fixed $\mathbf{x}$ coordinates is

$$\left.\frac{\partial \mathbf{u}_d}{\partial t}\right|_x = \mathcal{F}(\mathbf{u}_d, \mathbf{u}_p) - \nabla \pi \tag{2.51}$$

where

$$\begin{aligned} \mathcal{F}(\mathbf{u}_d, \mathbf{u}_p) &\equiv -\mathbf{A}(\mathbf{u}_d, \mathbf{u}_p) + \nu\Delta\mathbf{u} \\ \mathbf{A}(\mathbf{u}_d, \mathbf{u}_p) &\equiv \mathbf{u}\cdot\nabla\mathbf{u}_d + \mathbf{u}_d\cdot\nabla\mathbf{u}_p. \end{aligned} \tag{2.52}$$

Application of the transformation (2.15) results in an equation of motion for $u_d$ in mapped coordinates:

$$\left.\frac{\partial \mathbf{u}_d}{\partial t}\right|_\xi = \mathcal{F}(\mathbf{u}_d, \mathbf{u}_p) - \mathbf{F}^{-T}\nabla_\xi \pi \tag{2.53}$$

where the advection term has been redefined to include the relative convective derivative

$$\begin{aligned} \mathcal{F}(\mathbf{u}_d, \mathbf{u}_p) &\equiv -\mathbf{A}_s(\mathbf{u}_d, \mathbf{u}_p) + \nu\Delta\mathbf{u} \\ \mathbf{A}_s(\mathbf{u}_d, \mathbf{u}_p) &\equiv J^{-1}(\bar{\mathbf{u}}_d\cdot\nabla_\xi\mathbf{u}_p - ((\bar{\mathbf{u}}-\bar{\mathbf{s}})\cdot\nabla_\xi\mathbf{u}_d) \\ \pi &\equiv \left.\frac{\partial\phi}{\partial t}\right|_\xi - J^{-1}\bar{\mathbf{s}}\cdot\nabla_\xi(\mathbf{F}^{-T}\nabla_\xi\phi) + \frac{|\mathbf{u}_p|^2}{2} + p. \end{aligned} \tag{2.54}$$

Note that if the flow is frictionless and purely potential ($\mathbf{u} = \nabla\phi$), the equation of motion (2.53) reduces to Bernoulli's equation (2.30).

### Boundary Conditions

Another result of the splitting is resolution of viscous boundary conditions. Boundary conditions for the vortical velocity, $\mathbf{u}_d$, are obtained directly from the split-velocity relation $\mathbf{u}_d = \mathbf{u} - \mathbf{u}_p$, where $\mathbf{u}$ is given in (2.25-2.28) and $\mathbf{u}_p$ in (2.34-2.38):

(1) axis of symmetry

$$\mathbf{u}_d\cdot\mathbf{n} = 0, \tag{2.55}$$

(2) solid wall

$$\mathbf{u}_d\cdot\mathbf{n} = 0, \tag{2.56}$$

(3) inflow

$$\begin{aligned} u_d &= 0 \\ v_d &= 1 - 2r^2, \end{aligned} \tag{2.57}$$

(4) outflow

$$\frac{\partial \mathbf{u}_d}{\partial z} = 0. \tag{2.58}$$

The splitting is applied trivially to obtain a boundary condition at the axis (2.55). The inhomogeneous solid wall boundary condition is completely resolved in the BVP, yielding a desirable homogeneous relation for $\mathbf{u}_d$ (2.56). The inflow and outflow boundary conditions are derived in a more indirect way. At inflow, it is known that the velocity boundary condition is the classic parabolic profile of Poiseuille flow with mean flow of 1 (2.25). If the potential flow (constant plug flow of 1) is subtracted from the total flow, the result is a mean flow of 0 for the vortical component (2.57):

$$\int_{in} (\mathbf{u}_d \cdot \mathbf{n}) dr = 0. \tag{2.59}$$

This concept is also applied at outflow (2.58) where the mean flow is obtained from conservation of mass for a one-dimensional flow (2.38).

**Remarks on Splitting**

Hodge decomposition of the velocity splits the instationary incompressible Navier-Stokes equations (2.23) into two problems which are simpler to model: a BVP for the potential velocity with normal boundary conditions at any given state (time), and a well-posed IVP for the divergence-free component with homogeneous boundary conditions. The complication of a time-dependent incompressibility constraint remains an issue.

# Chapter 3

# Discretization of SV Formulation

The object of the SV formulation is to implement a discrete projection method for the incompressible Navier-Stokes equations where both the incompressibility constraint and boundary conditions are time-dependent. The split velocity allows use of the Hodge projection to enforce the constraint and compute the pressure–which is exactly what the projection is designed to do. It is desirable to discretize the equations of motion by the standard set in the second-order accurate BCG method.

This chapter describes the details of an algorithm designed from the SV formulation. First, a new time discretization which generalizes the BCG method is described in the context of a model problem. Second, there is a preliminary discussion of the discrete analogue of the analytical tools presented in the previous chapter needed to solve the problem. The problem domain is discretized based on moving, mapped grids for deformable boundaries. A discrete Hodge projection is the chosen method to evolve velocity and pressure while enforcing the incompressibility constraint. The bulk of the chapter is a detailed description of the time discretization of the SV algorithm. An SV version of the predictor-corrector method is outlined. Several issues involved in numerical implementation of the SV projection algorithm are also explained in detail.

**Equations of Motion**

In the previous chapter it was shown that a needed design criterion for the problem of flow in a flexible tube is a split velocity field which resolves the issue of inhomogeneous and time-dependent velocity boundary conditions. The potential flow solution is known at all times from the BVP which it satisfies

$$\nabla_\xi \cdot J\mathbf{F}^{-1}\mathbf{F}^{-T}\nabla_\xi \phi = 0 \tag{3.1}$$

with boundary conditions as specified in (2.34-2.38). The equations of motion for the divergence-free velocity are obtained by extracting the BVP for potential flow and defining a Bernoulli pressure:

$$\begin{aligned} \left.\frac{\partial \mathbf{u}_d}{\partial t}\right|_\xi &= \mathcal{F}(\mathbf{u}_d, \mathbf{u}_p) - \nabla\pi \\ \nabla_\xi \cdot (J\mathbf{F}^{-1}\mathbf{u}_d) &\equiv 0 \end{aligned} \tag{3.2}$$

where boundary conditions for $\mathbf{u}_d$ are specified in (2.55-2.58). The differential equations and incompressibility constraint reduce to a well-posed IVP, but there is still a problem with enforcement of a time-dependent constraint. A suitable discretization is desired to achieve this task.

## 3.1 A Model Problem

A model problem is discussed to address the issue of time-differentiation of the incompressibility constraint. The BCG method is a second-order accurate scheme for fixed domains where there is no complication with differentiation of the constraint. For a deformable domain, if the constraint is differentiated, the result is a complicated expression comprised of both the constrained quantity and its derivatives. Furthermore, it is difficult to implement the projection in the time-dependent case, and second-order accuracy is not known. The goal of the SV method is to extend the BCG method to time-dependent domains.

**A Model Problem**

The model problem is a general form of the equation of motion (2.53). Let $f, u \in \mathcal{R}^n$, $\pi \in \mathcal{R}^m$, $A = n \times m$ matrix where $u, A, f = u(t), f(t), A(t)$ are smooth functions in time. The constrained system is comprised of an equation of motion and a constraint, respectively:

$$\begin{aligned} \frac{du}{dt} &= f - A^T \pi \\ Au &= 0. \end{aligned} \tag{3.3}$$

$u$ is representative of velocity, in general. $f$ contains advection and viscosity terms in the case of an incompressible flow. $A$ and $A^T$ are adjoint matrix operators that correspond to divergence and gradient, for example, and include boundary conditions.

The constraint can be used to obtain an equation for $\pi$ in order to evolve the system exactly. To obtain this "pressure-Poisson" type equation, the constraint is differentiated and substituted into the divergence of the equation of motion:

$$\frac{d}{dt}(Au) = 0 \Longrightarrow \frac{dA}{dt}u + \frac{du}{dt}A = \frac{dA}{dt}u + Af - AA^T\pi. \tag{3.4}$$

The resulting equation for $\pi$ is

$$L\pi = Af + \frac{dA}{dt}u \tag{3.5}$$

where $L \equiv AA^T$. Solvability is assumed for (3.5). In the case of an incompressible fluid, either $L$ is invertible, or it has a null-space that is independent of time.

### 3.1.1 Predictor-Corrector Discretization

**BCG Method**

First, consider $A$ independent of time. Define operators $Q = A^T L^{-1} A$ and $P = I - Q$. These operators can be used to eliminate the constraint:

$$\frac{\partial u}{\partial t} = Pf. \tag{3.6}$$

In that case, the BCG discretization reduces to

$$u^{n+1} = u^n + \Delta t P(f^{n+\frac{1}{2}}) = P(u^n + \Delta t f^{n+\frac{1}{2}}) \tag{3.7}$$

where $\Delta t$ is the discrete time step. This discretization is inherently second-order due to use of the midpoint rule for $f$. Also, $P(u^{n+1}) = u^{n+1}$ if $P(u^n) = u^n$.

The BCG discretization can be written in predictor-corrector form:

$$\begin{aligned} u^* &= u^n + \Delta t(f^{n+\frac{1}{2}} - A^T \pi^{n-\frac{1}{2}}) \\ u^{n+1} &= P(u^*) \\ L(\pi^{n+\frac{1}{2}} - \pi^{n-\frac{1}{2}}) &= \frac{1}{\Delta t} A(u^n + \Delta t(f^{n+\frac{1}{2}} - A^T \pi^{n-\frac{1}{2}})) \end{aligned} \tag{3.8}$$

given $u^n, \pi^{n-\frac{1}{2}} \approx u(t^n), \pi(t^n - \frac{\Delta t}{2})$.

### SV Method

The SV method generalizes BCG for the model problem with time-dependent $A$. The corresponding discretization is

$$u^* = u^n + \Delta t(f^{n+\frac{1}{2}} - (A^{n+\frac{1}{2}})^T \pi^{n-\frac{1}{2}}) \tag{3.9}$$

$$u^{n+1} = P(u^*) = P(u^n + \Delta t(f^{n+\frac{1}{2}} - (A^{n+\frac{1}{2}})^T \pi^{n-\frac{1}{2}})), \tag{3.10}$$

$$L^{n+1}(\pi^{n+\frac{1}{2}} - \pi^{n-\frac{1}{2}}) = \frac{1}{\Delta t} A^{n+1}(u^n + \Delta t(f^{n+\frac{1}{2}} - (A^{n+\frac{1}{2}})^T \pi^{n-\frac{1}{2}})), \tag{3.11}$$

where all terms are evaluated at the discrete time, $t = t^{n+1}$, unless otherwise indicated.

### Accuracy of SV Method

Let $w^{new}, q^{new}$ be solutions approximated by the predictor-corrector scheme:

$$\begin{aligned} w^{new} &= P(w + \Delta t(f^{n+\frac{1}{2}} + (A^{n+\frac{1}{2}})^T q)) \\ q^{new} &= q + \frac{1}{\Delta t}(L^{n+1})^{-1} A^{n+1}(w + \Delta t(f^{n+\frac{1}{2}} + (A^{n+\frac{1}{2}})^T q). \end{aligned} \tag{3.12}$$

Define $u_e^n = u(t^n), \pi_e^{n+\frac{1}{2}} = \pi(t^{n+\frac{1}{2}})$ where $u, \pi$ are solutions to the model problem (3.3). If $w = u_e^n$ and $q = \pi_e^{n-\frac{1}{2}} + O(\Delta t)$, then

(1) the method is second-order accurate:

$$w^{new} = u_e^{n+1} + O(\Delta t^3) \tag{3.13}$$

and,

(2)

$$q^{new} = \pi_e^{n+\frac{1}{2}} + O(\Delta t). \tag{3.14}$$

**Proof of (1)**

In order to prove the consistency of the predictor-corrector discretization, the solution $w^{new}$ is compared to the standard of a Crank-Nicolson solution which employs the midpoint rule. It is noted that the midpoint rule for ordinary differential equations yields global second-order accuracy.

$$\begin{aligned} w^{mid} &\equiv u_e^n + \Delta t(f^{n+\frac{1}{2}} + (A^T\pi_e)^{n+\frac{1}{2}}) \\ &= u_e^{n+1} + O(\Delta t^3) \\ P^{n+1}w^{mid} &= w^{mid} + O(\Delta t^3) \\ w^{new} - w^{mid} &= \Delta t P^{n+1}(A^{n+\frac{1}{2}})^T(\pi_e^{n+\frac{1}{2}} - q) + O(\Delta t^3) \\ &= O(\Delta t^3) \end{aligned} \tag{3.15}$$

since $P^{n+1}(A^{n+\frac{1}{2}})^T$ is $O(\Delta t)$.

**Proof of (2)**

$$\begin{aligned} \pi^{new} &= q + (L^{n+1})^{-1}\left(\frac{A^{n+1} - A^n}{\Delta t}u_e^n + A^{n+1}f^{n+\frac{1}{2}} + A^{n+1}(A^{n+\frac{1}{2}})^T q\right) \\ &= (L^{n+1})^{-1}\left(\frac{A^{n+1} - A^n}{\Delta t}u_e^n + A^{n+1}f^{n+\frac{1}{2}}\right) + A^{n+1}(A^{n+\frac{1}{2}} - A^{n+1})^T q \\ &= \pi_e^{n+\frac{1}{2}} + O(\Delta t). \end{aligned} \tag{3.16}$$

Note that (2) depends only on $q$ being bounded independent of time, i.e., the proof begins with a statement of the truncation error and ends with the same statement.

**Remarks**

The predictor-corrector discretization requires the application of only a succession of fixed time operators rather than solution to problems resulting from differentiation of the constraint with respect to time. In this fashion, the solution always satisfies the constraint.

## 3.2 Discretization of Problem Domain

Discretization of the SV formulation for incompressible viscous flow on a deformable domain contains two main components: discretization of the problem domain which is the mechanism by which a deformable domain is modeled; and a time discretization for the projection formulation. The latter will be discussed in the next section. This section describes a finite difference approach to discretization of the problem domain using a moving quadrilateral grid.

**Finite Differences**

In order to approximate the derivatives, boundary conditions and the incompressibility constraint in the equations of motion, the spatial and temporal domains are discretized by finite differences. For spatial discretization, a grid is layed out over the spatial domain such that the center of each cell carries the integer indices $(i, j)$. Edges of cells are denoted by $(i+\frac{1}{2}, j)$ and $(i, j+\frac{1}{2})$. The indices of a cell vertex are $(i+\frac{1}{2}, j+\frac{1}{2})$. The discrete difference between two cells is either $\Delta r$ or $\Delta z$, depending on the direction of the gradient.

Time-centering is indicated by a superscript, $n$, corresponding to time $t = t^n$. Given a discrete solution at a time $t = t^n$, the solution is evolved to time $t = t^{n+1}$. The discrete difference in the evolved time is called a time step, $\Delta t = t^{n+1} - t^n$. The object of the numerical algorithm is to successively obtain a solution updated from the previous time increment until the desired final time is reached.

Discrete velocity is a cell-centered quantity and is represented as $U^n_{i,j}$. The vortical


**Figure 3.1:** Averaging operators.

component of velocity is also cell-centered, $U^n_{d,i,j}$. The potential velocity is a MAC, or edge-centered, velocity, $U^n_{p,i+\frac{1}{2},j}$, at a constant $\xi$ edge, for example. Pressure is a cell-centered term, $\pi^{n+\frac{1}{2}}_{i,j}$, which is centered at the half step in time, $t = t^n + \frac{\Delta t}{2}$. Averaging from cell-centers to cell-edges, and vice versa, is accomplished by operators $\mathbf{Av}^{C\to E}$ and $\mathbf{Av}^{E\to C}$, demonstrated graphically in Figure 3.1.

### Discrete Mapping

The transformation of coordinates (2.15) is used to model irregular domains which result from movement of the solid wall boundary. A mesh composed of quadrilaterals is placed on the real domain of the problem. A logically rectangular, computational space, $\boldsymbol{\xi}$, is mapped onto the physical space, $\mathbf{x}$ (see Figure 3.2). It is in the former space where the time-differencing and undivided spatial differencing take place.

Let the edge of each quadrilateral cell represent a tangent vector along a coordinate line (see Figure 3.3):

$$\begin{aligned}
\mathbf{t}^{\eta}_{i,j+\frac{1}{2}} &= \mathbf{x}_{\xi_{i,j+\frac{1}{2}}} = \mathbf{x}_{i+\frac{1}{2},j+\frac{1}{2}} - \mathbf{x}_{i-\frac{1}{2},j+\frac{1}{2}} \approx \Delta\xi \left.\frac{\partial \mathbf{x}}{\partial \xi}\right|_{i,j+\frac{1}{2}} \\
\mathbf{t}^{\xi}_{i+\frac{1}{2},j} &= \mathbf{x}_{\eta_{i+\frac{1}{2},j}} = \mathbf{x}_{i+\frac{1}{2},j+\frac{1}{2}} - \mathbf{x}_{i+\frac{1}{2},j-\frac{1}{2}} \approx \Delta\eta \left.\frac{\partial \mathbf{x}}{\partial \eta}\right|_{i+\frac{1}{2},j}.
\end{aligned} \tag{3.17}$$

Note that the partial derivatives in computational coordinates are undivided differences. Normal vectors can be defined from the tangents

$$\begin{aligned}
\mathbf{n}^{\eta}_{i,j+\frac{1}{2}} &= (-\mathrm{z}_{\xi}, \mathrm{r}_{\xi})_{i,j+\frac{1}{2}} \\
\mathbf{n}^{\xi}_{i+\frac{1}{2},j} &= (\mathrm{z}_{\eta}, -\mathrm{r}_{\eta})_{i+\frac{1}{2},j}
\end{aligned} \tag{3.18}$$

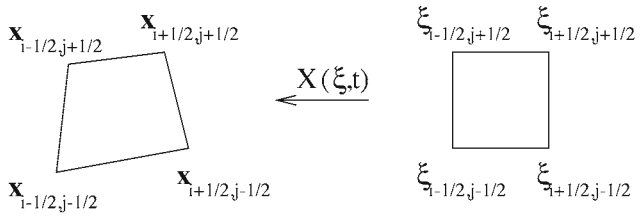


**Figure 3.2:** Discrete mapping. Time-dependent quadrilateral grid mapped into a fixed, rectangular grid.

and averaged to cell centers when needed:

$$\begin{aligned} \mathbf{n}^{\xi}_{i,j} &= \frac{1}{2}(\mathbf{n}^{\xi}_{i+\frac{1}{2},j} + \mathbf{n}^{\xi}_{i-\frac{1}{2},j}) \\ \mathbf{n}^{\eta}_{i,j} &= \frac{1}{2}(\mathbf{n}^{\eta}_{i,j+\frac{1}{2}} + \mathbf{n}^{\eta}_{i,j-\frac{1}{2}}). \end{aligned} \tag{3.19}$$

The volume metrics are similarly defined at cell edges:

$$\begin{aligned} g^{\eta}_{i,j+\frac{1}{2}} &= 2\pi r_{i,j+\frac{1}{2}} \\ g^{\xi}_{i+\frac{1}{2},j} &= 2\pi r_{i+\frac{1}{2},j}. \end{aligned} \tag{3.20}$$

These quantities can be averaged to cell centers in the same fashion as normals. Also, normals can be redefined to include the volume metrics at the respective edges on which they live, $\mathbf{n}_g = g\mathbf{n}$.

A discrete definition of the Jacobian of transformation, or cell volume, follows from the tangent equations and is used to calculate the quantity at the half step in time:

$$\sigma^{n+\frac{1}{2}}_{i,j} = g^{n+\frac{1}{2}}_{i,j}\left(\frac{1}{2}\left|\mathbf{t}^{\xi}_{i,j+\frac{1}{2}} \times \mathbf{t}^{\eta}_{i+\frac{1}{2},j}\right| + \frac{1}{2}\left|\mathbf{t}^{\xi}_{i,j-\frac{1}{2}} \times \mathbf{t}^{\eta}_{i-\frac{1}{2},j}\right|\right)^{n+\frac{1}{2}}. \tag{3.21}$$

The analytical form of the Jacobian is seen in its representation at a cell edge

$$\begin{aligned} \sigma_{i+\frac{1}{2},j} &= g^{\eta}_{i+\frac{1}{2},j}(r_{\xi_{i+\frac{1}{2},j}} z_{\eta_{i+\frac{1}{2},j}} - r_{\eta_{i+\frac{1}{2},j}} z_{\xi_{i+\frac{1}{2},j}}) \\ \sigma_{i,j+\frac{1}{2}} &= g^{\xi}_{i,j+\frac{1}{2}}(r_{\xi_{i,j+\frac{1}{2}}} z_{\eta_{i,j+\frac{1}{2}}} - r_{\eta_{i,j+\frac{1}{2}}} z_{\xi_{i,j+\frac{1}{2}}}) \end{aligned} \tag{3.22}$$

where metrics at other edges are obtained from the four "nearest neighbors":

$$\begin{aligned} \mathbf{x}_{\xi_{i+\frac{1}{2},j}} &= \frac{1}{4}(\mathbf{x}_{\xi_{i+1,j+\frac{1}{2}}} + \mathbf{x}_{\xi_{i+1,j-\frac{1}{2}}} + \mathbf{x}_{\xi_{i,j+\frac{1}{2}}} + \mathbf{x}_{\xi_{i,j-\frac{1}{2}}}) \\ \mathbf{x}_{\eta_{i,j+\frac{1}{2}}} &= \frac{1}{4}(\mathbf{x}_{\eta_{i+\frac{1}{2},j+1}} + \mathbf{x}_{\eta_{i-\frac{1}{2},j+1}} + \mathbf{x}_{\eta_{i+\frac{1}{2},j}} + \mathbf{x}_{\eta_{i-\frac{1}{2},j}}). \end{aligned} \tag{3.23}$$

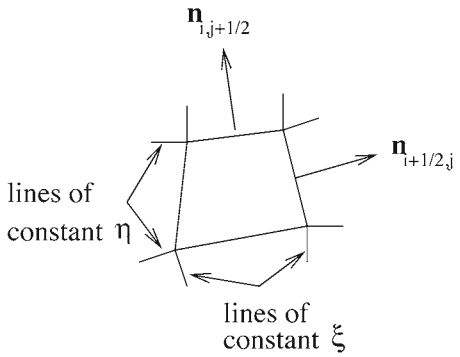


**Figure 3.3:** Cell volume, edge normals and indices.

The discrete Jacobian is evolved to a new time by conservation of volume [6]:

$$\sigma_{i,j}^{n+1} = \sigma_{i,j}^{n} + \delta\sigma_{i+\frac{1}{2},j}^{n+\frac{1}{2}} - \delta\sigma_{i-\frac{1}{2},j}^{n+\frac{1}{2}} + \delta\sigma_{i,j+\frac{1}{2}}^{n+\frac{1}{2}} - \delta\sigma_{i,j-\frac{1}{2}}^{n+\frac{1}{2}} \tag{3.24}$$

where $J_t = \nabla \cdot \mathbf{s}$, and

$$\begin{aligned} \delta\sigma_{i+\frac{1}{2},j}^{n+\frac{1}{2}} &= g_{i+\frac{1}{2},j}^{n+\frac{1}{2}} \Sigma(\mathbf{x}_{i+\frac{1}{2},j-\frac{1}{2}}^{n}, \mathbf{x}_{i+\frac{1}{2},j+\frac{1}{2}}^{n}, \mathbf{x}_{i+\frac{1}{2},j+\frac{1}{2}}^{n+1}, \mathbf{x}_{i+\frac{1}{2},j-\frac{1}{2}}^{n+1}) \\ \delta\sigma_{i,j+\frac{1}{2}}^{n+\frac{1}{2}} &= g_{i,j+\frac{1}{2}}^{n+\frac{1}{2}} \Sigma(\mathbf{x}_{i+\frac{1}{2},j+\frac{1}{2}}^{n}, \mathbf{x}_{i-\frac{1}{2},j+\frac{1}{2}}^{n}, \mathbf{x}_{i-\frac{1}{2},j+\frac{1}{2}}^{n+1}, \mathbf{x}_{i+\frac{1}{2},j+\frac{1}{2}}^{n+1}) \end{aligned} \tag{3.25}$$

are the partial cell volumes for a moving quadrilateral element (see Figure 3.4).

The inverse transformation matrix, $\mathbf{F}^{-1}$, is a matrix whose rows are made up of the components of the normals, $\mathbf{n}^{\xi}$ and $\mathbf{n}^{\eta}$:

$$\mathbf{F}^{-1} = gJ^{-1} \begin{bmatrix} z_{\eta} & -r_{\eta} \\ -z_{\xi} & r_{\xi} \end{bmatrix}. \tag{3.26}$$

The appropriate volume weighting of the inverse transformation is derived from the unrestricted three dimensional definition of the transformation matrix. To understand this quantity discretely, it must be placed into the correct context–namely, transformation of a vector in real coordinates to that in computational coordinates. Also, spatial centering of the inverse transformation is not trivial. These issues are addressed as needed in the discretization of the projection and in the details of the algorithm.

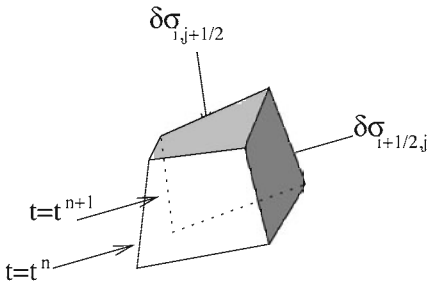


**Figure 3.4:** Representation of the time-dependence of $J$. Cell at $t^n$ moves to $t^{n+1}$ showing partial cell volumes.

### Remarks

It has been noted at several points in the discussion that the spatial differencing is undivided. Since the computational domain is an abstract space, a spatial difference in $\boldsymbol{\xi}$ has no physical meaning. However, if divided differencing were employed in transformation of the equations of motion, the same equations would be obtained due to cancellation of terms with the Jacobian. Therefore, undivided differencing is also chosen as a means to maintain simplicity in the discrete representation.

### Equations of Motion

The equations of motion (3.1-3.2) are discretized in mapped coordinates as defined by the mapping (2.15). The equation of motion for the discrete divergence-free component of velocity is

$$\left.\frac{\partial U_d}{\partial t}\right|_{\xi} = \mathcal{F}(U_d, U_p) - \mathbf{F}^{-T}\nabla_{\xi}\pi \tag{3.27}$$

with the incompressibility constraint

$$\nabla_{\xi} \cdot (J\mathbf{F}^{-1}U_d) \equiv 0 \tag{3.28}$$

where

$$\mathcal{F}(U_d, U_p) \equiv -\mathbf{A}_s(U_d, U_p) + \nu J^{-1}\nabla_{\xi} \cdot (J\mathbf{F}^{-1}\mathbf{F}^{-T}\nabla_{\xi}U). \tag{3.29}$$

The relative advection term and Bernoulli pressure are defined as follows:

$$\begin{aligned} \mathbf{A}_s(U_d, U_p) &\equiv J^{-1}(\bar{U}_d \cdot \nabla_\xi U_p - ((\bar{U} - \bar{S}) \cdot \nabla_\xi U_d) \\ \pi &\equiv \left.\frac{\partial \phi}{\partial t}\right|_x + \frac{|U_p|^2}{2} + p \end{aligned} \tag{3.30}$$

where $\bar{U} = J\mathbf{F}^{-T}U$, $\bar{U}_d = J\mathbf{F}^{-T}U_d$ and $\bar{S} = J\mathbf{F}^{-T}S$ are transformed velocities. The boundary conditions for the discrete vortical velocity are given in (2.55-2.58).

The potential flow solution, $U_p = \nabla\phi$, is obtained from the BVP which it satisfies:

$$\Delta\phi = 0 \tag{3.31}$$

where the inhomogeneous normal boundary conditions of the problem are specified in (2.34-2.38).

## 3.3 Time Discretization

This section discusses the time-stepping procedure used in the SV projection method. Any time step in the SV algorithm begins with the knowledge of a cell-centered velocity, $U^n_{d,i,j}$, at time $t^n$, and a cell-centered Bernoulli pressure, $\pi^{n-\frac{1}{2}}_{i,j}$, at the lagged time, $t^{n-\frac{1}{2}}$. Also, the potential velocity, $U_p$, is known at all times from the discrete Dirichlet problem which it satisfies; therefore, the entire velocity is known prior to each time step. Evolution of the dependent variables is predicated upon a known initial solution which satisfies the boundary conditions and the incompressibility constraint.

### 3.3.1 Predictor-Corrector Discretization

The discrete vortical velocity is evolved by a predictor-corrector type scheme. A velocity is predicted from advection and viscosity terms, then updated, or corrected, by the projection operator to enforce incompressibility and to obtain the pressure. This procedure follows the temporal discretization discovered in the model problem.

### Predictor

The predictor part of the method is motivated by the desire to avoid solution to an implicit equation for $U_d$ which results from Crank-Nicolson differencing of the discrete equation of motion (3.27):

$$\left.\frac{U_d^{n+1} - U_d^n}{\Delta t}\right|_\xi = -\mathbf{A}_s(U_d, U_p)^{n+\frac{1}{2}} + \frac{\nu}{2}\left((\mathbf{L}_\nu U)^{n+1} + (\mathbf{L}_\nu U)^n\right) - \nabla^{n+\frac{1}{2}}\pi^{n+\frac{1}{2}}. \quad (3.32)$$

Instead, Crank-Nicolson differencing is applied to the Navier-Stokes equations for the entire velocity field in order to first approximate the viscous forces at $t^{n+\frac{1}{2}}$:

$$U^* = U_d^n + U_p^{n+1} + \Delta t\left(-\mathbf{A}_s(U_d, U_p)^{n+\frac{1}{2}} + \frac{\nu}{2}\left(\mathbf{L}_\nu^{n+1}(U^*) + \mathbf{L}_\nu^n(U^n)\right) - \nabla^{n+\frac{1}{2}}\pi^{n-\frac{1}{2}}\right) \quad (3.33)$$

where $U^*$ is an intermediate velocity approximating $U^{n+1}$ and is not necessarily divergence-free. $U^*$ is obtained by solving a form of the heat equation:

$$(\mathbf{I} - \frac{\nu\Delta t}{2}\mathbf{L}_\nu^{n+1})U^* = RHS. \quad (3.34)$$

The right-hand side, $RHS$, to this diffusion equation is given from (3.33):

$$RHS = U_d^n + U_p^{n+1} + \Delta t\left(-\mathbf{A}_s(U_d, U_p)^{n+\frac{1}{2}} + \frac{\nu}{2}\mathbf{L}_\nu^n(U^n) - \nabla^{n+\frac{1}{2}}\pi^{n-\frac{1}{2}}\right). \quad (3.35)$$

A predicted vortical component of velocity, which is not necessarily divergence-free, is then obtained from (3.33), given $U^*$:

$$U_{d,i,j}^{**} = U_{i,j}^* - U_{p,i,j}^{n+1}. \quad (3.36)$$

It is also noted that the pressure lags in time at $t^{n-\frac{1}{2}}$ in the predictor; however, the gradient operating on the lagged pressure is centered at the appropriate half time $t^{n+\frac{1}{2}}$.

### Corrector

From analysis of discretization of the model problem earlier in this chapter, the discrete form of the vortical corrector for $U_d$ is a projection centered at time $t^{n+1}$ of the predicted vortical velocity, $U_d^{**}$:

$$U_d^{n+1} = \mathbf{P}^{n+1}(U_d^{**}). \quad (3.37)$$

The projection form of this equation suggests solution to the following Poisson's equation in pressure correction form:

$$\mathbf{L}^{n+1}(\Delta t \delta_{i,j}) = \mathbf{D}_0 U^{**}_{d,i,j} \tag{3.38}$$

where the pressure correction is $\delta = \pi^{n+\frac{1}{2}} - \pi^{n-\frac{1}{2}}$. Once the pressure correction is obtained, the cell-centered gradient is computed and used to update the divergence-free velocity:

$$\begin{aligned} U^{n+1}_{d,i,j} &= U^{**}_{d,i,j} - \mathbf{G}^{n+1}_0 \delta_{i,j} \\ \pi^{n+\frac{1}{2}}_{i,j} &= \pi^{n-\frac{1}{2}}_{i,j} + \frac{\delta_{i,j}}{\Delta t}. \end{aligned} \tag{3.39}$$

Finally, the entire updated velocity field is calculated by adding the updated divergence-free component to the potential velocity at $t^{n+1}$ which has been averaged to cell centers:

$$U^{n+1}_{i,j} = U^{n+1}_{d,i,j} + \mathbf{Av}^{E\to C} U^{n+1}_p. \tag{3.40}$$

**Outline of Discretization Issues**

An outline of the issues involved in discretizing each piece of the projection formulation is as follows:

(1) Discretization of projection operator.

(2) Potential flow solution.

(3) Convective discretization.

(4) Solvers.

### 3.3.2 Discretization of Projection Operator

The discrete Hodge projection operator, $\mathbf{P}$, is defined in the same manner as the continuous projection. The goal is to resolve a vector into its divergence-free and gradient parts:

$$\begin{aligned} W &= W_d + G\phi \\ DW_d &= 0 \end{aligned} \tag{3.41}$$

where $\mathbf{G}$ and $\mathbf{D}$ represent the finite difference approximations to gradient and divergence, respectively. The projection is applied by the following procedure:

(1) Solve

$$L\phi = DW \tag{3.42}$$

(2) Compute

$$W_d = W - G\phi \tag{3.43}$$

where $L = DG$ is the discrete Laplacian operator.

The choice of $D$ and $G$ determine the strength of the projection. If they are chosen as discrete adjoints, $D = -G^T$, then $\mathbf{P} = \mathbf{P}^T$. Also, the discrete Hodge projection operator is idempotent: $\mathbf{P} = \mathbf{P}^2$. The two previous statements about $\mathbf{P}$ imply its boundedness:

$$\|\mathbf{P}(W)\| \leq \|W\| \tag{3.44}$$

where $\|\|$ is the discrete $L_2$ norm derived from the vector inner product

$$\begin{aligned} \langle U, V \rangle &= \Sigma_{i,j}(U_{i,j} \cdot V_{i,j})\Delta x \Delta y \\ \|Q\| &= \langle Q, Q \rangle^{\frac{1}{2}}. \end{aligned} \tag{3.45}$$

Some drawbacks of discrete projections for co-located discretizations of the velocity field are documented in [1, 39].

### BCG-MAC Discretization of P

MAC, or "marker and cell", discretization of the projection operator is an idempotent, discrete representation of the projection. Idempotence of the projection is shown by the relation, $\mathbf{P}^2 = \mathbf{P}$, or more specifically, by the invertibility of the Laplacian operator, $\mathbf{L}$:

$$\begin{aligned} \mathbf{P} &= (\mathbf{I} - \mathbf{G}^{MAC}\mathbf{L}^{-1}\mathbf{D}^{MAC}) \\ \mathbf{L} &= \mathbf{D}^{MAC}\mathbf{G}^{MAC}. \end{aligned} \tag{3.46}$$

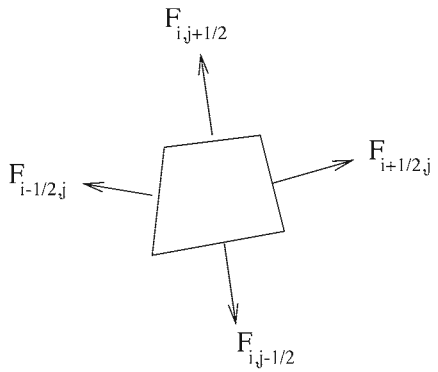


**Figure 3.5:** Finite volume description of divergence. $F = U \cdot \mathbf{n}_g$ is the flux at an edge of a cell.

The MAC projection is a cell-edge based discretization. The divergence operator, $\mathbf{D}^{MAC}$, is discretized based on a finite volume approach for calculation of conservation of mass within a cell (see Figure 3.5):

$$(\nabla \cdot U)_{i,j} = \left( (\mathbf{n}_g \cdot U)_{i+\frac{1}{2},j} - (\mathbf{n}_g \cdot U)_{i-\frac{1}{2},j} + (\mathbf{n}_g \cdot U)_{i,j+\frac{1}{2}} - (\mathbf{n}_g \cdot U)_{i,j-\frac{1}{2}} \right) / \sigma_{i,j} \quad (3.47)$$

where $\mathbf{n}_g = g\mathbf{n}$ is the volume normal. Another perspective of the MAC discretization of divergence can be seen by rigorous application of the mapping

$$(\nabla \cdot U)_{i,j} = (J^{-1} \nabla_\xi \cdot J\mathbf{F}^{-1} U)_{i,j} = (J^{-1} \nabla_\xi \cdot \bar{U})_{i,j} \quad (3.48)$$

or,

$$(\nabla \cdot U)_{i,j} = (\bar{u}_{i+\frac{1}{2},j} - \bar{u}_{i-\frac{1}{2},j} + \bar{v}_{i,j+\frac{1}{2}} - \bar{v}_{i,j-\frac{1}{2}}) / \sigma_{i,j} \quad (3.49)$$

where the transformed velocity is specially defined at edges as

$$\begin{aligned} \bar{u}_{i+\frac{1}{2},j} &= g^{\xi}_{i+\frac{1}{2},j} \mathbf{n}^{\xi}_{i+\frac{1}{2},j} \cdot U_{i+\frac{1}{2},j} \\ \bar{v}_{i,j+\frac{1}{2}} &= g^{\eta}_{i,j+\frac{1}{2}} \mathbf{n}^{\xi}_{i,j+\frac{1}{2}} \cdot U_{i,j+\frac{1}{2}}. \end{aligned} \quad (3.50)$$

An undivided difference in the $\boldsymbol{\xi}$ gradient has been dotted into a transformed velocity whose two components are defined at edges which are described by a constant $\xi$ or a constant $\eta$ line, respectively (refer again to Figure 3.3). The spatial centering of the inverse

transformation matrix is seen in this relation where the rows of $\mathbf{F}^{-1}$ are made up of the normals at corresponding edges.

The MAC gradient follows from $\nabla\phi = \mathbf{F}^{-T}\nabla_\xi\phi$:

$$\begin{aligned}
\mathbf{G}^{MAC}\phi_{i+\frac{1}{2},j} &= \frac{g^\xi}{\sigma}\begin{bmatrix} z_\eta & -z_\xi \\ -r_\eta & r_\xi \end{bmatrix}_{i+\frac{1}{2},j}\begin{bmatrix} \phi_{i+1,j} - \phi_{i,j} \\ \frac{1}{4}(\phi_{i+1,j+1} + \phi_{i,j+1} - \phi_{i+1,j-1} - \phi_{i,j-1}) \end{bmatrix} \\
\mathbf{G}^{MAC}\phi_{i,j+\frac{1}{2}} &= \frac{g^\eta}{\sigma}\begin{bmatrix} z_\eta & -z_\xi \\ -r_\eta & r_\xi \end{bmatrix}_{i,j+\frac{1}{2}}\begin{bmatrix} \frac{1}{4}(\phi_{i+1,j+1} + \phi_{i+1,j} - \phi_{i-1,j+1} - \phi_{i-1,j}) \\ \phi_{i+1,j} - \phi_{i,j} \end{bmatrix}
\end{aligned} \tag{3.51}$$

Boundary conditions are applied to $\mathbf{L}$ when the stencil for the MAC gradient extends beyond the problem domain. At edges coming out from boundaries, $\phi$ is extrapolated into a "ghost" cell to calculate the transverse component of $\nabla_\xi\phi$. For example, at the $i = \frac{1}{2}$ edge,

$$\phi_{0,j} = 3(\phi_{1,j} - \phi_{2,j}) + \phi_{3,j} \tag{3.52}$$

where the subscript 0 denotes the ghost cell value.

### Approximate Projection Operator

An approximate projection was developed to remove the drawbacks of discrete projections pertaining to complications which result from centering and linear algebra (see [1, 39] for details). In an approximate projection, the discrete divergence of velocity does not exactly satisfy incompressibility: $DU = O(h^2)$. The approximate projection operator, $\mathbf{P}$, involves cell-centered discretizations of $D$ and $G$. The choice of cell-centered discretization of $\mathbf{P}$ leads to a non-idempotent projection, $\mathbf{P}^2 \neq \mathbf{P}$, where $\mathbf{P} = (\mathbf{I} - \mathbf{G}_0\mathbf{L}^{-1}\mathbf{D}_0)$. The exact Laplacian operator as defined in the MAC discretization is not invertible with $\mathbf{P}$, i.e., $\mathbf{D}_0\mathbf{G}_0 \neq \mathbf{L}$, where $\mathbf{L} = \mathbf{D}^{MAC}\mathbf{G}^{MAC}$, $\mathbf{D}_0 = \mathbf{D}^{MAC}\mathbf{Av}^{C\to E}$ and $\mathbf{G}_0 = \mathbf{Av}^{E\to C}\mathbf{G}^{MAC}$. Therefore, the incompressibility constraint is only approximately satisfied.

The cell-centered divergence operator, $\mathbf{D}_0$, is a MAC divergence operator that is simply applied to a cell-centered velocity which has been averaged to edges by the operator $\mathbf{Av}^{C\to E}$, making the cell-centered velocity a MAC velocity. However, the cell-centered gradient

operator, $G_0$, is a more complicated discretization. The procedure for computing $\mathbf{G}_0\phi_{i,j}$, which involves application of the averaging operator $\mathbf{Av}^{E\to C}$, is as follows:

(1) Compute the MAC gradients, $\mathbf{G}^{MAC}\phi_{i+\frac{1}{2},j}$ and $\mathbf{G}^{MAC}\phi_{i,j+\frac{1}{2}}$, on interior edges.

(2) Extrapolate the vectors $\mathbf{G}^{MAC}\phi_{i+\frac{1}{2},j}$, $\mathbf{G}^{MAC}\phi_{i,j+\frac{1}{2}}$ linearly to boundaries.

(3) Compute $\mathbf{n}\cdot\mathbf{G}^{MAC}\phi$ at all edges.

(4) Compute $\mathbf{G}_0\phi_{i,j}$ by solving the following equations:

$$\begin{aligned}\mathbf{n}^{\xi}_{i,j}\cdot\mathbf{G}_0\phi_{i,j} &= [(\mathbf{n}\cdot\mathbf{G}^{MAC}\phi)_{i+\frac{1}{2},j}+(\mathbf{n}\cdot\mathbf{G}^{MAC}\phi)_{i-\frac{1}{2},j}]/2 = a^{\xi}_{i,j}\\ \mathbf{n}^{\eta}_{i,j}\cdot\mathbf{G}_0\phi_{i,j} &= [(\mathbf{n}\cdot\mathbf{G}^{MAC}\phi)_{i,j+\frac{1}{2}}+(\mathbf{n}\cdot\mathbf{G}^{MAC}\phi)_{i,j-\frac{1}{2}}]/2 = a^{\eta}_{i,j}\end{aligned}$$

$$\Longrightarrow \mathbf{G}_0\phi_{i,j} = \frac{1}{(r_\xi z_\eta - r_\eta z_\xi)_{i,j}}\begin{bmatrix} r_\xi & r_\eta \\ z_\xi & z_\eta\end{bmatrix}_{i,j}\begin{bmatrix} a^{\xi} \\ a^{\eta}\end{bmatrix}_{i,j} \tag{3.53}$$

where the normals do not carry volume implications.

Boundary conditions for MAC gradients in the cell-centered calculation are a linear extrapolation of $\mathbf{G}^{MAC}\phi$ from interior edges:

$$\mathbf{G}^{MAC}\phi_{\frac{1}{2},j} = 2\mathbf{G}^{MAC}\phi_{\frac{3}{2},j} - \mathbf{G}^{MAC}\phi_{\frac{5}{2},j}, \tag{3.54}$$

for example, at the axis of symmetry boundary edge, $i=\frac{1}{2}$.

### Discrete Laplacian Operator

The Laplacian operator is based upon a nine-point stencil for quadrilateral grids. The stencil is the same throughout the algorithm with the only variation being boundary conditions on $\nabla\phi$. If the Laplacian of $\phi$ at cell $(i,j)$ is written as the sum of coefficients multiplied by $\phi_{i,j}$ and its nearest neighbors,

$$\mathbf{L}\phi_{i,j} = \frac{1}{\sigma_{i,j}}\Sigma a_{\vec{s}}\phi_{\vec{i}+\vec{s}}, \tag{3.55}$$

then the stencil coefficients, $a_{\vec{s}}$, are as follows:

$$\begin{aligned}
a_{-1,1} &= ((G^\xi s)_{i-\frac{1}{2},j} + (G^\eta s)_{i,j+\frac{1}{2}})/4 \\
a_{0,1} &= (-(G^\xi s)_{i+\frac{1}{2},j} + (G^\xi s)_{i-\frac{1}{2},j})/4 + (G^\eta l^\xi)_{i,j+\frac{1}{2}} \\
a_{1,1} &= (-(G^\xi s)_{i+\frac{1}{2},j} - (G^\eta s)_{i,j+\frac{1}{2}})/4 \\
a_{-1,0} &= ((G^\eta s)_{i,j+\frac{1}{2}} - (G^\eta s)_{i,j-\frac{1}{2}})/4 + (G^\xi l^\eta)_{i-\frac{1}{2},j} \\
a_{0,0} &= -(G^\xi l^\eta)_{i-\frac{1}{2},j} - (G^\xi l^\eta)_{i+\frac{1}{2},j} - (G^\eta l^\xi)_{i,j+\frac{1}{2}} - (G^\eta l^\xi)_{i,j-\frac{1}{2}} \\
a_{1,0} &= (-(G^\eta s)_{i,j+\frac{1}{2}} + (G^\eta s)_{i,j-\frac{1}{2}})/4 + (G^\xi l^\eta)_{i+\frac{1}{2},j} \\
a_{-1,-1} &= (-(G^\xi s)_{i-\frac{1}{2},j} - (G^\eta s)_{i,j-\frac{1}{2}})/4 \\
a_{0,-1} &= ((G^\xi s)_{i+\frac{1}{2},j} - (G^\xi s)_{i-\frac{1}{2},j})/4 + (G^\eta l^\xi)_{i,j-\frac{1}{2}} \\
a_{1,-1} &= ((G^\xi s)_{i+\frac{1}{2},j} + (G^\eta s)_{i,j-\frac{1}{2}})/4
\end{aligned} \tag{3.56}$$

where

$$\begin{aligned}
G^\xi &\equiv \frac{g^\xi}{r_\xi z_\eta - r_\eta z_\xi} \\
G^\eta &\equiv \frac{g^\eta}{r_\xi z_\eta - r_\eta z_\xi} \\
l^\xi &\equiv r_\xi^2 + z_\xi^2 \\
l^\eta &\equiv r_\eta^2 + z_\eta^2 \\
s &\equiv r_\xi r_\eta + z_\xi z_\eta.
\end{aligned} \tag{3.57}$$

### Viscosity Operator

The viscosity operator, $\mathbf{L}_\nu$, possesses the same stencil as the discrete Laplacian operator, $\mathbf{L}$, on the interior, but differs at the boundaries where physical boundary conditions are applied:

(1) axis of symmetry

$$\begin{aligned}
u^* &= 0 \\
\frac{\partial v^*}{\partial z} &= 0,
\end{aligned} \tag{3.58}$$

(2) solid wall (higher-order extrapolation with prescribed wall velocity)

$$\begin{aligned} U^*|_{wall} &= U_b^{n+1} \\ U^* &= a\xi^2 + b\xi + c \\ \left.\frac{\partial U^*}{\partial \xi}\right|_{wall} &= b = -3U_{Nr}^* + \frac{1}{3}U_{Nr-1}^* + \frac{8}{3}U_b^{n+1} \\ \left.\frac{\partial U^*}{\partial \eta}\right|_{wall} &= \frac{\partial U_b^{n+1}}{\partial \eta}, \end{aligned} \tag{3.59}$$

(3) inflow (Poiseuille flow applied with higher order extrapolation)

$$\begin{aligned} u^* &= 0 \\ v^* &= 2(1-r^2), \end{aligned} \tag{3.60}$$

(4) outflow

$$\frac{\partial U^*}{\partial z} = 0. \tag{3.61}$$

At the axis of symmetry, there is no flow across the axis in the normal direction; the transverse component takes a homogeneous Neumann boundary condition (3.58). At the moving solid wall, a higher-order boundary condition is chosen which is exact for Poiseuille flow in an initially fixed, straight tube (3.59). The inflow boundary condition is Poiseuille flow (3.60). At outflow, a homogeneous Neumann condition is set on $U^*$ in the $z$-direction– the normal direction at the outlet since the grid is orthogonal (3.61).

### 3.3.3 Potential Flow Solution

The first application of the discrete projection operator is the potential flow problem. The potential flow solution is critical to the SV method for it is this component of the total velocity which carries the burden of time-dependent boundary conditions. The potential velocity, $U_p = \nabla\phi$, can be obtained at any time, $t^n$, given the special boundary conditions for $U^n$ at inflow and outflow, and the prescribed velocity of the solid wall. The solution is

obtained by solution to the Poisson's equation

$$\mathbf{L}^n \phi = 0 \tag{3.62}$$

where the operator, $\mathbf{L}$, has a homogeneous Neumann boundary condition at all boundaries

$$\mathbf{n} \cdot \nabla \phi = 0 \tag{3.63}$$

and the boundary conditions for the solution are given in (2.34-2.38).

Once the solution to Poisson's equation is found, the MAC gradient is applied to the potential to obtain the MAC potential velocity:

$$U_p^n = \mathbf{G}^{MAC,n} \phi. \tag{3.64}$$

The MAC velocities can be averaged to cell-centers when needed using the previously described averaging operator. Boundary conditions for the MAC gradients are extrapolated as in the cell-centered gradient calculation discussed earlier in this chapter.

### 3.3.4 Convective Discretization

The nonlinear, convective derivative, $\mathbf{A}_s(U_d, U_p)^{n+\frac{1}{2}}$, in (3.27) is calculated using a second-order Godunov method with a MAC projection [4, 39]. First, the cell-centered velocity, $U_{d,i,j}^n$, is extrapolated to cell edges and to the half step in time by Taylor series expansion, omitting the effect of pressure. A MAC projection is then used to enforce the incompressibility constraint on $U_d^{n+\frac{1}{2}}$. Nonconservative differencing is used to approximate $\mathbf{A}_s(U_d, U_p)^{n+\frac{1}{2}}$. There is a time step restriction for the entire algorithm because of the explicit convective discretization.

#### Taylor Extrapolation

The discrete divergence-free velocity, $U_{d,i,j}^n$, is expanded to the half step in time, $t^n + \frac{\Delta t}{2}$, and to cell edges in a Taylor series (see Figure 3.6):

$$\hat{U}_{d,i+\frac{1}{2},j}^{n+\frac{1}{2}} = U_{d,i,j}^n + \frac{\Delta \xi}{2} \frac{\partial U_d}{\partial \xi}^{n+\frac{1}{2}} + \frac{\Delta t}{2} \left. \frac{\partial U_d}{\partial t} \right|_{\xi}^{n+\frac{1}{2}}. \tag{3.65}$$

$\left.\frac{\partial U_d}{\partial t}\right|_\xi$ (without the pressure gradient) is then substituted from (3.27) into (3.65). The velocities at constant $\xi$ edges are extrapolated from cell-centered values to the left (denoted by $L$) and to the right ($R$) of an edge:

$$\begin{aligned}
\hat{U}^{n+\frac{1}{2},L}_{d,i+\frac{1}{2},j} &= U^n_{i,j} + \frac{1}{2}\left(1 - \bar{u}^{upw,n}_{s,i,j}\frac{\Delta t}{\sigma^n_{i,j}}\right)\frac{\partial U_d}{\partial \xi}^n_{i,j} - \frac{\Delta t}{2}\left(\frac{\bar{v}^n_{i,j}}{\sigma^n_{i,j}}\right)\left[\frac{\partial U_d}{\partial \eta}\right]^n_{i,j} \\
&\quad -\frac{\Delta t}{2}\left(\bar{u}^n_{d,i,j}\frac{\partial U_p}{\partial \xi}^n_{i,j} + \bar{v}^n_{d,i,j}\frac{\partial U_p}{\partial \eta}^n_{i,j}\right) - \frac{\nu\Delta t}{2}\mathbf{L}^n_\nu U^n_{i,j} \\
\hat{U}^{n+\frac{1}{2},R}_{d,i+\frac{1}{2},j} &= U^n_{i+1,j} - \frac{1}{2}\left(1 + \bar{u}^{upw,n}_{s,i+1,j}\frac{\Delta t}{\sigma^n_{i+1,j}}\right)\frac{\partial U_d}{\partial \xi}^n_{i+1,j} + \frac{\Delta t}{2}\left(\frac{\bar{v}^n_{i+1,j}}{\sigma^n_{i+1,j}}\right)\left[\frac{\partial U_d}{\partial \eta}\right]^n_{i+1,j} \\
&\quad +\frac{\Delta t}{2}\left(\bar{u}^n_{d,i,j}\frac{\partial U_p}{\partial \xi}^n_{i,j} + \bar{v}^n_{d,i,j}\frac{\partial U_p}{\partial \eta}^n_{i,j}\right) + \frac{\nu\Delta t}{2}\mathbf{L}^n_\nu U^n_{i,j}. \qquad (3.66)
\end{aligned}$$

Velocities are computed in a similar manner at constant $\eta$ edges where the directions $L$ and $R$ are referred to the subscript $j$:

$$\begin{aligned}
\hat{U}^{n+\frac{1}{2},L}_{d,i,j+\frac{1}{2}} &= U^n_{i,j} + \frac{1}{2}\left(1 - \bar{v}^{upw,n}_{i,j}\frac{\Delta t}{\sigma^n_{i,j}}\right)\frac{\partial U_d}{\partial \eta}^n_{i,j} - \frac{\Delta t}{2}\left(\frac{\bar{u}^n_{s,i,j}}{\sigma^n_{i,j}}\right)\left[\frac{\partial U_d}{\partial \xi}\right]^n_{i,j} \\
&\quad -\frac{\Delta t}{2}\left(\bar{u}^n_{d,i,j}\frac{\partial U_p}{\partial \xi}^n_{i,j} + \bar{v}^n_{d,i,j}\frac{\partial U_p}{\partial \eta}^n_{i,j}\right) - \frac{\nu\Delta t}{2}\mathbf{L}^n_\nu U^n_{i,j} \\
\hat{U}^{n+\frac{1}{2},R}_{d,i,j+\frac{1}{2}} &= U^n_{i,j+1} - \frac{1}{2}\left(1 + \bar{v}^{upw,n}_{i,j+1}\frac{\Delta t}{\sigma^n_{i,j+1}}\right)\frac{\partial U_d}{\partial \eta}^n_{i,j+1} + \frac{\Delta t}{2}\left(\frac{\bar{u}^n_{s,i,j+1}}{\sigma^n_{i,j+1}}\right)\left[\frac{\partial U_d}{\partial \xi}\right]^n_{i,j+1} \\
&\quad +\frac{\Delta t}{2}\left(\bar{u}^n_{d,i,j}\frac{\partial U_p}{\partial \xi}^n_{i,j} + \bar{v}^n_{d,i,j}\frac{\partial U_p}{\partial \eta}^n_{i,j}\right) + \frac{\nu\Delta t}{2}\mathbf{L}^n_\nu U^n_{i,j}. \qquad (3.67)
\end{aligned}$$

A transformed "upwind" velocity is used for the convective velocity in the extrapolated velocity calculations to ensure that only known information about the convecting velocity has been called upon:

$$\begin{aligned}
\bar{u}^{upw}_s &= max(\bar{u} - \bar{s}, 0) \\
\bar{v}^{upw} &= max(\bar{v}, 0). \qquad (3.68)
\end{aligned}$$

where the subscript $s$ indicates inclusion of the relative motion due to the grid movement.

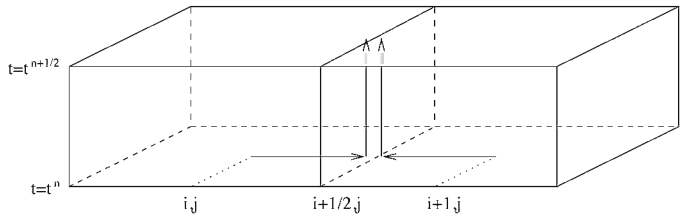


**Figure 3.6:** Godunov box depicting extrapolation of cell-centered velocities to edges and to the half step in time.

### Slopes

The slopes in the normal direction of the spatial expansion in the Taylor extrapolation are approximated by centered differences with one-sided differences at the boundary:

$$\begin{aligned} \frac{\partial U_d}{\partial \xi}^n_{i,j} &\approx \frac{U_{d,i+1,j} - U_{d,i-1,j}}{2} \\ \frac{\partial U_d}{\partial \eta}^n_{i,j} &\approx \frac{U_{d,i,j+1} - U_{d,i,j-1}}{2}. \end{aligned} \tag{3.69}$$

A second-order van Leer method could be used to limit the normal slopes. This technique has not been employed here in order to obtain clean convergence results [31].

The slopes in the tranverse direction are given by

$$\begin{aligned} \left[\frac{\partial U_d}{\partial \xi}\right]^n_{i,j} &\approx \begin{cases} \hat{U}^n_{d,i,j} - \hat{U}^n_{d,i-1,j} & \text{if } (\bar{u}^n_{i,j} - \bar{s}^n_{i,j}) \geq 0 \\ \hat{U}^n_{d,i+1,j} - \hat{U}^n_{d,i,j} & \text{if } (\bar{u}^n_{i,j} - \bar{s}^n_{i,j}) < 0 \end{cases} \\ \left[\frac{\partial U_d}{\partial \eta}\right]^n_{i,j} &\approx \begin{cases} \hat{U}^n_{d,i,j} - \hat{U}^n_{d,i,j-1} & \text{if } \bar{v}^n_{i,j} \geq 0 \\ \hat{U}^n_{d,i,j+1} - \hat{U}^n_{d,i,j} & \text{if } \bar{v}^n_{i,j} < 0 \end{cases} \end{aligned} \tag{3.70}$$

with an instability correction for the diffusive, viscous term pointed out by Minion [45]:

$$\hat{U}^n_{d,i,j} = U^n_{d,i,j} + \frac{\nu \Delta t}{2} \Delta U^n_{i,j}. \tag{3.71}$$

The slopes of the potential velocity are calculated from MAC quantities:

$$\begin{aligned} \frac{\partial U_p}{\partial \xi}^n_{i,j} &\approx U_{p,i+\frac{1}{2},j} - U_{p,i-\frac{1}{2},j} \\ \frac{\partial U_p}{\partial \eta}^n_{i,j} &\approx U_{p,i,j+\frac{1}{2}} - U_{p,i,j-\frac{1}{2}}. \end{aligned} \tag{3.72}$$

### Riemann Problem

At each cell edge, a Riemann problem exists where there is a left and right state from which to choose based on the upwind, convective velocity:

$$\hat{U}^{n+\frac{1}{2}}_{d,i+\frac{1}{2},j} = \begin{cases} U^L_d & \text{if } \bar{u}^{upw,l}_s, \bar{u}^{upw,r}_s > 0 \\ U^R_d & \text{if } \bar{u}^{upw,l}_s, \bar{u}^{upw,r}_s < 0 \\ \frac{U^L_d + U^R_d}{2} & \text{if } \bar{u}^{upw,l}_s \bar{u}^{upw,r}_s \leq 0 \end{cases} \tag{3.73}$$

$$\hat{U}^{n+\frac{1}{2}}_{d,i,j+\frac{1}{2}} = \begin{cases} U^L_d & \text{if } \bar{v}^{upw,l}, \bar{v}^{upw,r} > 0 \\ U^R_d & \text{if } \bar{v}^{upw,l}, \bar{v}^{upw,r} < 0 \\ \frac{U^L_d + U^R_d}{2} & \text{if } \bar{v}^{upw,l} \bar{v}^{upw,r} \leq 0 \end{cases} \tag{3.74}$$

where these upwind, convective velocities are defined as

$$\begin{aligned} \bar{u}^{upw,l}_s &\equiv (U^n_{i,j} - S^{n+\frac{1}{2}}_{i+\frac{1}{2},j}) \cdot \mathbf{n}^{\xi n+\frac{1}{2}}_{i+\frac{1}{2},j} \\ \bar{u}^{upw,r}_s &\equiv (U^n_{i+1,j} - S^{n+\frac{1}{2}}_{i+\frac{1}{2},j}) \cdot \mathbf{n}^{\xi n+\frac{1}{2}}_{i+\frac{1}{2},j} \\ \bar{v}^{upw,l} &\equiv (U^n_{i,j} - S^{n+\frac{1}{2}}_{i,j+\frac{1}{2}}) \cdot \mathbf{n}^{\eta n+\frac{1}{2}}_{i,j+\frac{1}{2}} \\ \bar{v}^{upw,r} &\equiv (U^n_{i,j+1} - S^{n+\frac{1}{2}}_{i,j+\frac{1}{2}}) \cdot \mathbf{n}^{\eta n+\frac{1}{2}}_{i,j+\frac{1}{2}}. \end{aligned} \tag{3.75}$$

The boundary conditions for the upwinded, extrapolated MAC velocities are the prescribed conditions for $U_d$ (2.55-2.58). At boundaries where the condition is of Neumann form, the extrapolated left or right state–whichever is on the interior side of the boundary edge–is used.

### MAC Projection

The MAC velocities are projected in order to account for the effect of the pressure gradient at $t^{n+\frac{1}{2}}$ which was omitted in the Taylor extrapolation:

$$\mathbf{L}\phi^{n+\frac{1}{2}}_{i,j} = \mathbf{D}^{\mathbf{MAC}}\hat{U}^{n+\frac{1}{2}}. \tag{3.76}$$

The MAC velocities are corrected by MAC gradients accordingly:

$$\begin{aligned} U^{n+\frac{1}{2}}_{d,i+\frac{1}{2},j} &= \hat{U}^{n+\frac{1}{2}}_{d,i+\frac{1}{2},j} - \nabla\phi^{n+\frac{1}{2}}_{i+\frac{1}{2},j} \\ U^{n+\frac{1}{2}}_{d,i,j+\frac{1}{2}} &= \hat{U}^{n+\frac{1}{2}}_{d,i,j+\frac{1}{2}} - \nabla\phi^{n+\frac{1}{2}}_{i,j+\frac{1}{2}}. \end{aligned} \tag{3.77}$$

Boundary conditions for the MAC gradients are homogeneous Neumann, $\mathbf{n} \cdot \nabla\phi = 0$, at all boundaries except outflow where the boundary condition is homogeneous Dirichlet. This is discretized by setting the ghost cell value, $\phi_0 = -\phi_1$.

**Nonconservative Differencing**

The nonlinear, convective derivative, $\mathbf{A}_s = (U - S) \cdot \nabla U_d + U_d \cdot \nabla U_p$, is calculated using nonconservative differencing:

$$((U - S) \cdot \nabla U_d)_{i,j}^{n+\frac{1}{2}} = \frac{1}{\sigma_{i,j}^{n+\frac{1}{2}}} \left( \bar{u}_{s,i,j}^{n+\frac{1}{2}} \frac{\partial U_d}{\partial \xi} + \bar{v}_{i,j}^{n+\frac{1}{2}} \frac{\partial U_d}{\partial \eta} \right) \tag{3.78}$$

where

$$\begin{aligned} \bar{u}_{s,i,j}^{n+\frac{1}{2}} &= \frac{1}{2}(\bar{u}_{s,i+\frac{1}{2},j}^{n+\frac{1}{2}} + \bar{u}_{s,i-\frac{1}{2},j}^{n+\frac{1}{2}}) \\ \bar{v}_{i,j}^{n+\frac{1}{2}} &= \frac{1}{2}(\bar{v}_{i,j+\frac{1}{2}}^{n+\frac{1}{2}} + \bar{v}_{i,j-\frac{1}{2}}^{n+\frac{1}{2}}) \\ \frac{\partial U_d}{\partial \xi} &= U_{d,i+\frac{1}{2},j}^{n+\frac{1}{2}} - U_{d,i-\frac{1}{2},j}^{n+\frac{1}{2}} \\ \frac{\partial U_d}{\partial \eta} &= U_{d,i,j+\frac{1}{2}}^{n+\frac{1}{2}} - U_{d,i,j-\frac{1}{2}}^{n+\frac{1}{2}}. \end{aligned} \tag{3.79}$$

The solid wall boundary condition is $\bar{u}_s^{n+\frac{1}{2}}\Big|_{wall} = 0$ because $U \cdot \mathbf{n}|_{wall} = S \cdot \mathbf{n}|_{wall}$.

The part of $\mathbf{A}_s$ due to the potential velocity is similarly calculated:

$$(U_d \cdot \nabla U_p)_{i,j}^{n+\frac{1}{2}} = \frac{1}{\sigma_{i,j}^{n+\frac{1}{2}}} \left( \bar{u}_{d,i,j}^{n+\frac{1}{2}} \frac{\partial U_p}{\partial \xi} + \bar{v}_{d,i,j}^{n+\frac{1}{2}} \frac{\partial U_p}{\partial \eta} \right) \tag{3.80}$$

where

$$\begin{aligned} \bar{u}_{d,i,j}^{n+\frac{1}{2}} &= \frac{1}{2}(\bar{u}_{d,i+\frac{1}{2},j}^{n+\frac{1}{2}} + \bar{u}_{d,i-\frac{1}{2},j}^{n+\frac{1}{2}}) \\ \bar{v}_{d,i,j}^{n+\frac{1}{2}} &= \frac{1}{2}(\bar{v}_{d,i,j+\frac{1}{2}}^{n+\frac{1}{2}} + \bar{v}_{d,i,j-\frac{1}{2}}^{n+\frac{1}{2}}) \\ \frac{\partial U_p}{\partial \xi} &= U_{p,i+\frac{1}{2},j}^{n+\frac{1}{2}} - U_{p,i-\frac{1}{2},j}^{n+\frac{1}{2}} \\ \frac{\partial U_p}{\partial \eta} &= U_{p,i,j+\frac{1}{2}}^{n+\frac{1}{2}} - U_{p,i,j-\frac{1}{2}}^{n+\frac{1}{2}}. \end{aligned} \tag{3.81}$$

### Time Step Restriction

The second-order Godunov method is an explicit scheme. The time step of the entire algorithm is dependent upon the Courant-Friedrichs-Lewy (CFL) condition for stability:

$$\Delta t = .9/\max_{i,j}\left(\frac{|\bar{u}_{i,j} - \bar{s}_{i,j}|}{\sigma_{i,j}}, \frac{|\bar{v}_{i,j}|}{\sigma_{i,j}}\right) \tag{3.82}$$

where the transformed velocity, $\bar{U} = J\mathbf{F}^{-1}U$, is centered component-wise as follows:

$$\begin{aligned} \bar{u}_{i,j} &= g_{i,j}(z_{\eta_{i,j}} u_{i,j} - r_{\eta_{i,j}} v_{i,j}) \\ \bar{v}_{i,j} &= g_{i,j}(-z_{\xi_{i,j}} u_{i,j} + r_{\xi_{i,j}} v_{i,j}). \end{aligned} \tag{3.83}$$

## 3.3.5 Solvers

### Multigrid

Each time step of the SV method requires solution to five Poisson's equations: two potential flow solutions, one at time $t^{n+\frac{1}{2}}$ and the other at time $t^{n+1}$; a MAC projection at time $t^{n+\frac{1}{2}}$; solution to the heat equation for the viscous terms; and an approximate projection at time $t^{n+1}$. Solution to Poisson's equation throughout the algorithm is obtained by multigrid iterations. The multigrid method is a technique used to solve a linear system like $L\phi = f$ without the expense of inverting the linear operator $L$. (See [10] for an introduction to this method and [37, 36, 39] for details concerning projection methods.)

In the SV algorithm the primary issue concerning multigrid is coarsening of the quadrilateral grid and metrics. Quadrilateral elements are maintained in coarsening of the grid as demonstrated in Figure 3.7. The $r$ and $z$ coordinates at coarser levels are the correct values, but loss of detail in the geometry at domain boundaries is evident. Also, the cell volume, $\sigma_{coarse}$, is computed on coarser levels by averaging the values of $\sigma_{fine}$ from contributing fine grid cells as opposed to a calculation of volume from coarse coordinates; thus, conservation of volume of the mesh is preserved:

$$\sigma_{coarse} = \Sigma\sigma_{fine}. \tag{3.84}$$

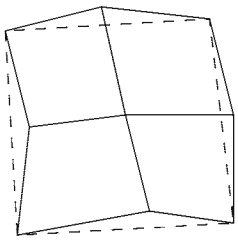

**Figure 3.7:** Grid coarsening. Solid lines indicate fine grid cells and dotted lines indicate coarse grid cell.

Averaging of the residual, $\mathcal{R}$, to coarser levels is done in the following manner:

$$\mathcal{R}_{coarse} = \frac{\Sigma(\mathcal{R}\sigma)_{fine}}{\sigma_{coarse}}. \tag{3.85}$$

The iteration scheme on any level is Gauss-Seidel with red-black ordering. For iteration $l$ this means

$$\phi_{i,j}^{l+1} = \phi_i j^l - \frac{1}{\lambda_{i,j}} \left( L_{i,j}\phi_i j^l - f_{i,j} \right) \tag{3.86}$$

where the relaxation parameter, $\lambda_{i,j}$, is defined to be the diagonal coefficients of the linear operator $L_{i,j}$. The algorithm features a full multigrid V-Cycle for accelerated convergence and maximum coarsening [10]. At the coarsest level, an optimal number of Gauss-Seidel iterations with red-black ordering are performed.

### Implementation of Projection

Consider the following Poisson's equation and its graphic representation in Figure 3.8:

$$\mathbf{L}\phi = \nabla \cdot \mathcal{F}. \tag{3.87}$$

In general, the potential, $\phi$, is composed of a homogeneous part, $\phi_H$, and an inhomogeneous part, $\phi_B$:

$$\phi = \phi_H + \phi_B. \tag{3.88}$$

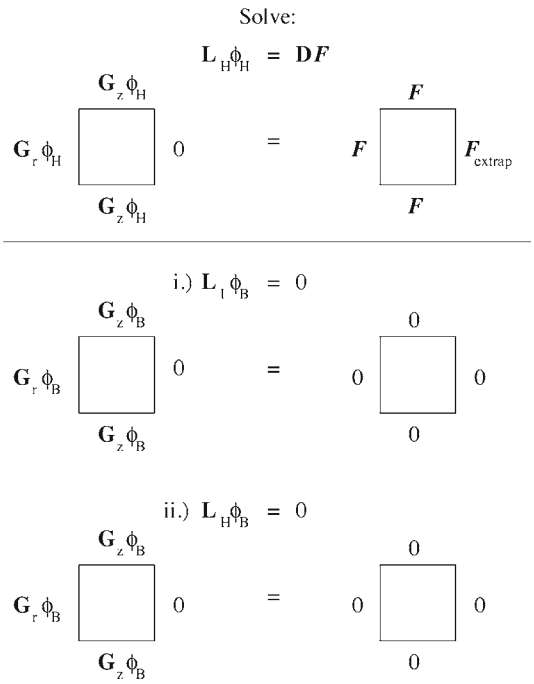


**Figure 3.8:** Discrete representation of solution to Poisson's equation.

$\phi_H$ is the solution to the homogeneous problem

$$\begin{aligned} \mathbf{L}_H \phi_H &= \nabla \cdot \mathcal{F} \\ \frac{\partial \phi_H}{\partial n} &= 0 \end{aligned} \tag{3.89}$$

with homogeneous boundary conditions for $\mathbf{L}_H$ and extrapolated boundary conditions for the flux of $\mathcal{F}$ in the divergence. The other part, $\phi_B$, satisfies the inhomogeneous problem

$$\begin{aligned} \mathbf{L}_I \phi_B &= 0 \\ \frac{\partial \phi_B}{\partial n} &= \mathcal{H} \\ \mathcal{H} &= \mathbf{n} \cdot \mathcal{F} \end{aligned} \tag{3.90}$$

where $\mathcal{H}$ is an inhomogeneous boundary condition which contains the normal component of the extrapolated piece of $\mathcal{F}$ from the divergence flux at the boundary in the homogeneous step. The inhomogeneous problem is rewritten into an equivalent one for the homogeneous operator by transferring the inhomogeneity in $\mathbf{L}_I$ to the right-hand side of the equation (see

Figure 3.8):

$$\begin{aligned} \mathbf{L}_H \phi_B &= \nabla \cdot (-\mathcal{H}) \\ \frac{\partial \phi_B}{\partial n} &= 0. \end{aligned} \tag{3.91}$$

The homogeneous problem and the equivalent inhomogeneous problem can now be added into one discrete equation since the same operator, $\mathbf{L}_H$, is used in both:

$$\mathbf{L}_H \phi = \mathbf{D}(\mathcal{F} - \mathcal{H}). \tag{3.92}$$

**Remarks**

A key observation in the numerical implementation of the projection is that the extrapolated boundary condition for the divergence of $\tilde{\mathcal{F}}$ is consumed in the pressure and is never seen in the actual discretization. Also, desirable homogeneous boundary conditions are applied to fluxes of $\tilde{\mathcal{F}}$ in the divergence at boundaries since the pressure is carrying the extrapolated piece. See also Lai [39] for a slightly different discussion on this topic.

# Chapter 4

# Results and Conclusions

The final chapter presents the results obtained by the SV algorithm for unsteady incompressible flows in a flexible tube. First, results for the inviscid case of potential flow are presented and explained. Treatment of time-dependent boundary conditions described in previous chapters is made clear. Next, laminar flow scenarios are presented for an incompressible viscous fluid in a flexible tube with inlet Reynolds numbers of 8, 16, 200, 400 and 800. Relevant physics is discussed for simple boundary motions. The chapter concludes with details of the robustness of the model by explanation of features which can be represented in other flow scenarios. Future applications of the model are also brought forward.

### Grid Generation

Grid generation is a concern when modeling a deformable domain by the method of moving, mapped grids. The grid has to be regenerated each time step in the SV algorithm for a moving solid wall boundary. This is accomplished by linear interpolation between the axis of symmetry at $r = 0$ and the solid wall at $r = R(z)$. The grid does not move in the $z$-direction for any of the prescribed boundary movements that test the algorithm–all deformation of the grid occurs radially.

There is a local loss in accuracy of the velocity at the axis, mostly seen in the radial component, attributed to the linear interpolation used in regridding the mesh. The trend

is that the radial component of velocity loses an order of accuracy locally at the axis of symmetry without affecting the overall convergence rate. The loss in accuracy is seen at locations in $z$ along the axis where deformation has occurred in the solid wall across the flow; the more the solid wall deforms, the more the error approaches first-order in terms of the computational mesh spacing $h$ (see Figures 4.2 and 4.3 ). The degree of loss in accuracy also varies somewhat with the Reynolds number, but no definite conclusions can be made.

## 4.1 Accuracy

Results for the various flow scenarios are discussed in terms of known exact solutions, qualitative features from the physics of the flow and numerical accuracy. The SV method presented is designed to capture the details of flow dynamics in time, especially near boundaries. Both spatial and temporal numerical accuracy is to be maintained at second-order while modeling the proper physics of the flow. Numerical accuracy is measured in terms of the decrease in error with refinement of grid spacing. Exact solutions are known in certain cases and can be used in the validation process in the absence of empirical data.

### Convergence Rate

A convergence rate for the algorithm is calculated by estimating the error on successively refined grids:

$$e^h = \|avg(\varphi^{h/2}) - \varphi^h\|. \tag{4.1}$$

Superscripts refer to the mesh spacing of the grid. The norm, $\|\|$, is represented by the discrete $L_1$, $L_2$ or $L_\infty$ norm:

$$\|\Psi\|_{L_1} = \Sigma_{i,j}(\sigma_{i,j}|\Psi_{i,j}|) \tag{4.2}$$

$$\|\Psi\|_{L_2} = \left(\Sigma_{i,j}(\sigma_{i,j}|\Psi_{i,j}|^2)\right)^{1/2} \tag{4.3}$$

$$\|\Psi\|_{L_\infty} = max_{i,j}|\Psi_{i,j}|. \tag{4.4}$$

The averaging operator is defined with volume weighting:

$$avg(\varphi^h)_{i,j} = \frac{\sigma^h_{2i,2j}\varphi^h_{2i,2j} + \sigma^h_{2i+1,2j}\varphi^h_{2i+1,2j} + \sigma^h_{2i,2j+1}\varphi^h_{2i,2j+1} + \sigma^h_{2i+1,2j+1}\varphi^h_{2i+1,2j+1}}{\sigma^h_{2i,2j} + \sigma^h_{2i+1,2j} + \sigma^h_{2i,2j+1} + \sigma^h_{2i+1,2j+1}}. \quad (4.5)$$

The convergence rate (order of accuracy), $\alpha$, of the method is determined by the formula

$$\alpha = \frac{log\left(\frac{e^h}{e^{2h}}\right)}{log2}. \quad (4.6)$$

## 4.2 Incompressible Flow in a Flexible Tube

The SV method has been designed to model unsteady incompressible flows in a flexible tube. Results from models of inviscid and viscous flows are presented for a range of laminar Reynolds numbers and a variety of solid wall boundary motions. All calculations have been performed with the precision of 64 bit arithmetic. The convergence tolerance of the solvers in the algorithm is $(N_r \times N_z)10^{-14}$ times the initial error of the residual.

### 4.2.1 Potential Flow

The inviscid flow case described in chapter two has revealed much information about incompressible viscous flows with time-dependent boundaries, especially outflow. It is the potential velocity that carries the normal boundary conditions for these unsteady flows on deformable domains in the SV method. The potential flow solution is known at all times given prescribed conditions at inflow and solid walls. Furthermore, potential flow has no time history, but with time-dependent boundary conditions and without introduction of vorticity, the potential flow solution is the solution to the incompressible Euler equations.

#### Inward/Outward Hump

Consider a potential flow where the boundary moves from an inward to an outward Gaussian hump:

$$R(t) = R_0(1 - \epsilon(1 - \sin\pi(.5 + t)))exp^{(-4(z-z_c)^2)}. \quad (4.7)$$

| Case | $e^{1/16}$ | Rate | $e^{1/32}$ | Rate | $e^{1/64}$ |
|---|---|---|---|---|---|
| u | 9.56e-4 | 1.97 | 2.43e-4 | 1.98 | 6.15e-5 |
| v | 8.31e-4 | 1.98 | 2.11e-4 | 2.00 | 5.28e-5 |

**Table 4.1:** Convergence rates in $L_2$ norm for potential flow in flexible tube with inward and outward moving hump.

At times when the boundary is not moving ($t = 0$ and $t = 1.0$), symmetry in the radial component is shown (see top diagrams in Figure 4.4). In the axial component, due to expansion in the tube, negative velocity is calculated at outflow (see bottom diagrams in Figure 4.4 at $t = 0.5$). Conservation is held from start to finish where acceleration and deceleration of the potential flow are depicted at the beginning and end, respectively. Numerically, the velocity is second-order accurate in all norms (see Table 4.1, for example) with the exception of a first-order loss in accuracy in the $L_\infty$ norm at the axis due to grid generation.

### 4.2.2 Viscous Flow

This section discusses results obtained from the robust capabilities of the SV method for incompressible viscous flow in a flexible tube. Two flow regimes are featured: a low speed (high viscosity) flow, and a high speed (low viscosity) flow for Reynolds number well into the laminar regime. The Reynolds number is defined as $Re = \frac{\bar{v}d}{\nu}$ where $\bar{v}$ is the mean velocity, $d$ is the diameter of the tube ($d = 2$ in all cases) and $\nu$ is the kinematic viscosity.

The flow is initialized to the Poiseuille flow in a fixed tube:

$$u = 0 \tag{4.8}$$

$$v = 2\bar{v}(1 - r^2) \tag{4.9}$$

$$p = -8\bar{v}\nu z. \tag{4.10}$$

The boundary movement depicted for these flows is a periodically, inward moving hump from a straight tube at time $t = 0$ to a fully pinched (25 percent radial reduction) tube at

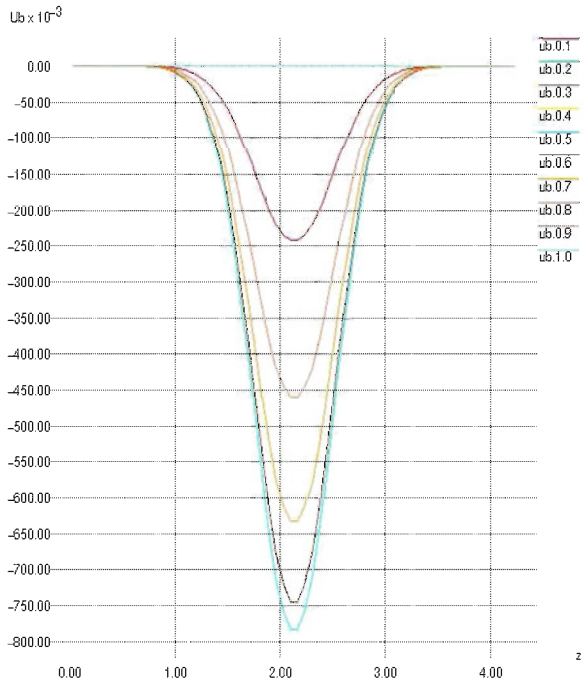


**Figure 4.1:** Periodic cycle for solid wall boundary velocity (not the grid movement itself). Boundary velocity is initially 0 at $t = 0$, reaches a maximum at $t = .5$ and returns to 0 at $t = 1$.

$t = 1.0$ (see Figure 4.1).

For the $Re = 8$ flow, the mean inlet velocity, $\bar{v}$, is 1 and the kinematic viscosity, $\nu$, is .25; for $Re = 200$, inlet velocity is the same and the kinematic viscosity is .01. For cases where the hump is moved outward ($Re = 16,400$), $\bar{v}$ is increased to 2 which doubles the Reynolds number. This is done to ensure that there is no backflow at outflow. For the $Re = 800$ case, $\bar{v} = 2$ and $\nu = .005$. The SV method yields a total velocity which is second-order accurate in time and space (see Tables 4.2 and 4.3, for example).

### Inward Moving Hump

For low Reynolds number, smooth features of the flow dynamics are maintained throughout the inward movement portion of the cycle (see Figures 4.5, 4.6, 4.7). As the boundary reaches its fullest extent inward, separation of the flow is noted beyond the hump at times $t = .9$ and $t = 1.0$. The flow reattaches downstream before the fluid exits the tube.

| Case | $e^{1/16}$ | Rate | $e^{1/32}$ | Rate | $e^{1/64}$ |
|---|---|---|---|---|---|
| u | 4.93e-3 | 1.60 | 1.63e-3 | 1.84 | 4.54e-4 |
| v | 3.66e-2 | 2.39 | 7.02e-3 | 2.27 | 2.70e-3 |

**Table 4.2:** Convergence rates in $L_2$ norm for unsteady, incompressible viscous flow. Results obtained for inlet $Re = 8$ at $t = .5$ when tube has been pinched to .875 of original radius.

| Case | $e^{1/16}$ | Rate | $e^{1/32}$ | Rate | $e^{1/64}$ |
|---|---|---|---|---|---|
| u | 1.97e-1 | 2.29 | 4.03e-2 | 1.93 | 1.06e-2 |
| v | 3.22e-1 | 1.87 | 8.81e-2 | 1.86 | 2.43e-2 |

**Table 4.3:** Convergence rates in $L_2$ norm for unsteady, incompressible viscous flow. Results obtained for inlet $Re = 200$ at $t = 1$ when tube is fully pinched, or .75 of original radius.

Snapshots in time of vorticity depict this flow phenomenon clearly (see Figure 4.5). The axial component does become negative along the boundary past the hump demonstrating detached flow, but reattachment is not seen as clearly due to the scaling (see Figure 4.6). Downstream, the axial velocity becomes positive again which signals reattachment. Second-order convergence of the numerical error for this flow is shown in Figure 4.2.

For higher Reynolds number, smooth features are maintained as well, but the velocity gradients are much steeper. Plot of vorticity does not seem to demonstrate much at early time, particularly due to the scaling (see Figure 4.8). At later time, however, flow separation is seen and eventually there exists complete detachment out the tube. Furthermore, a recirculation zone curls up just beyond the hump within the layer of separation. This phenomenon is seen more clearly in the axial component of velocity at late time (see Figure 4.9). The colormap of the figures depicts steep gradients in the axial velocity near the wall, especially at late time. This will be discussed further for the expanding tube. Second-order convergence of the numerical error for this flow is depicted in Figure 4.3.

### Outward Moving Hump

For the tube to expand back to its straight position, the Reynolds number must be doubled to eliminate total backflow at outflow. For the lower Reynolds number case, $Re = 16$, the flow separates and reattaches for the first part of expansion. It completely reattaches with no separation by the time it stops, nearly returning to Poiseuille flow (see Figure 4.11a). Remnants of the grid movement are blown out the end of the tube if the flow is allowed to achieve the viscous steady state by halting the grid movement. For the higher Reynolds number case, where there is separation and recirculation at $t = 1.0$, more violent vortical structures remain in the flow after expansion of the tube (see Figure 4.11b).

The interesting feature for all flow cases is the effect of vortical and potential components of velocity on the total velocity. The axial velocity is the most revealing parameter for this analysis because of familiarity with the classic parabolic Poiseuille profile for viscous flow in a pipe. Furthermore, it is of interest to see the effect of boundary conditions applied through the potential velocity compared to the vorticity-bearing divergence-free component of velocity. Figures 4.12, 4.13 are a breakdown of the total axial velocity and its vortical and potential parts at critical times in the pinching and expansion of the tube for low Reynolds number. At $t = .5$, the velocity profile is close to the classic Poiseuille parabola. The effects of the inward moving hump on the vortical component are clearly seen at the hump and downstream near the wall. Also, the increase in average axial velocity past the hump is shown in the potential component. At $t = 1.0$, the velocity profile becomes steeper near the wall and flatter over the top. The gradient of velocity has increased due to higher shear stress at the wall. Separation and reattachment occur just downstream from the hump midpoint. The boundary has come to rest at this time. The potential component depicts this well as the flow rate into the tube is the flow rate out of the tube with no added flux at the wall.

At time $t = 1.5$, the reverse effect from $t = .5$ seems to be occurring (see Figure 4.13).

The potential flow demonstrates a slowing down of the fluid past the hump because of tube expansion. This is seen in the average axial velocity as well. At this snapshot in time the viscous effects are being felt primarily before the hump. At the final time $t = 2.0$, the flow nearly returns to the steady viscous flow as it started. It is worth noting the plug flow contribution of potential flow to total velocity at $t = 2.0$.

In the higher Reynolds number case, the effects of vortical and potential velocity are unmistakable (see Figures 4.14, 4.15). At $t = .5$, the flow is highly vortical near the wall; away from the wall the flow is driven by potential flow. The velocity profile is much steeper near the wall than in the lower Reynolds number case. At the later time $t = 1.0$, the profile takes on a "top-hat" shape–nearly flat at the top, then it dips down and back up in an overshoot before it falls sharply at the boundary. (The "top-hat" profile is a design standard used in experiments to achieve stable behavior in jets [41, 42].) It is also worth noting that the vortical velocity shows a void in the center part of the tube. This is also seen (but only slightly due to scaling) at $t = 1.0$ for $Re = 8$ in Figure 4.6.

As the tube expands back outward for the higher Reynolds number flow, more interesting dynamics are depicted (see Figure 4.15). At $t = 1.5$, the void seen at $t = 1.0$ remains. Also, a shear layer forms. The divergence-free component reveals a separate vortical structure from the concentrated area at the hump. The recirculation zone lingers and extends out the tube. The velocity profile dips into the negative regime which is indicative of separation that has occurred before the hump. When the tube returns to the fixed, straight position at $t = 2.0$, the vortical component demonstrates that the flow is far from a viscous steady state even though the total axial velocity looks nearly like Poiseuille flow due to scaling. An artifact of the void noted before and what remains of a shear layer are also depicted.

Finally, a complete cycle of the movement of the hump is seen in Figure 4.16. The most notable feature in this flow scenario is a very sharp gradient which is captured in the axial component of the velocity at time $t = 3.5$, when the hump is moving back inward from its fully expanded outward position. The strong gradient, which indicates the presence of a

shear layer, exists in the axial direction as well as the familiar radial direction. Another observation is movement of the point of separation which is indicated in the axial component by a change in sign from positive to negative. As the hump expands outward from the flat position at time $t = 2.0$, the separation point marches from a location before the midpoint of the hump toward the inlet. In general, the combined effect of potential flow in an expanding tube and a high Reynolds number has been demonstrated to provide for interesting fluid dynamics.

## 4.3 Concluding Remarks

### Thesis Summary

A numerical method is presented that solves incompressible viscous flow in a tube with a deformable boundary. Chapter one gave the background of methods and problems which have led to the development of the SV algorithm. Specifically, it is Chorin's projection method with the second-order accurate predictor-corrector of Bell, Colella and Glaz upon which this work is built. It was noted that projection methods have been particularly successful at modeling the incompressible Navier-Stokes equations. The introductory chapter goes on to say that finite difference methods have worked well on irregular domains by the use of both immersed boundaries and mapped grids, as well as other methods.

In chapter two, the mathematical modeling issues for an incompressible viscous flow on a deformable domain are discussed. The incompressible Navier-Stokes equations were presented for the physical problem of flow through a flexible tube. The physical model was then transformed into a mathematical model via several mathematical tools. The Hodge decomposition was described and its concepts extended to the projection operator which yielded an evolution equation for the equations of motion. The fixed domain problem was briefly described and proposed to be well-posed because of the ability to differentiate the boundary conditions. Then the technique of moving, mapped grids was put forth for

handling a deformable domain. The inability to differentiate time-dependent boundary conditions was noted as the main issue for flow on deformable domains. This would lead to problems with enforcement of the incompressibility constraint.

The chapter continued as model of flow in a flexible tube was constructed. The inviscid case was explored in order to discover a solution to an unsolvable outflow boundary condition in the viscous case. The boundary value problem of potential flow was discussed as a special case. The Hodge decomposition, in conjunction with findings from the inviscid case–particularly, the restriction of a flat outlet section which yields a solution to the outflow problem–led to a split-velocity formulation where the velocity field is split into two components: the vortical component and the potential component. The vortical component of velocity enforces the incompressibility constraint in time by definition since it is divergence-free. The potential component is the solution to a BVP defined by normal boundary conditions and is known at all times. The splitting fits well into the framework of the projection. However, application of the constraint remained an issue.

In chapter three, a new time discretization which generalizes the BCG method was described. A model problem was explained, and a predictor-corrector method was shown to be second-order accurate. The SV method does not differentiate the incompressibility constraint, but, rather, applies only a succession of fixed time operators. In this fashion, the solution always satisfies the constraint. Also, the new discretization projects velocity, not acceleration.

The details of the SV algorithm discretization were completely offered in chapter three. Various numerical tools were first presented. With a discrete mapping it was shown how the transformation behaves in time. Discretizations for the projection operator were then put forward noting the exactness of the edge-based MAC projection and the approximate, but stable, cell-centered projection. Solution to the special case of potential flow was described as it is part of the flow that is to be known at all times.

Chapter three continued with the actual discretization of the algorithm. First, the sec-

ond order Godunov method with a MAC projection was described to obtain the nonlinear convective derivative. The viscous terms were then predicted by solving a diffusion equation based on the convective derivative and gradient of a lagged Bernoulli pressure with Crank-Nicholson differencing. The vortical velocity was then predicted and corrected by a cell-centered approximate projection using pressure correction formulation. The Bernoulli pressure was updated to the proper time centering as well. Finally, the total velocity was computed by adding the cell-centered potential part to the vortical part. Discrete implementation was outlined where solution to an inhomogeneous boundary value problem is broken down into a homogeneous interior problem and an equivalent inhomogeneous boundary problem, but solved as one. The multigrid iterative method was briefly described as a solver for Poisson's equation, with special attention given to grid coarsening.

The thesis has concluded with chapter four–a presentation and discussion of results obtained by the SV method. First, grid generation was described. A way of studying accuracy was then given with a note on loss of accuracy in the radial component of velocity at the axis of symmetry. Potential flow was shown and validated based on knowledge of exact solutions. The main results presented were the viscous flow simulations for an inward and outward moving hump in a tube. Numerical accuracy was shown to be second-order and several identifying characteristics of the modeled physics were captured. Separation and reattachment were shown for lower Reynolds number regimes. Separation and recirculation were demonstrated for higher Reynolds numbers. The balance between vortical and potential components of velocity was seen near and away from the boundary. The "top-hat" velocity profile of an internal laminar jet was also computed by the algorithm. Strong gradients resulting from shear layers were captured in the interior of the flow for expansion of the tube which validated the use of a compressible flow advection scheme.

**Future Work**

The initial goal of this thesis was to develop a numerical model of a true fluid-solid interaction. The fluid dynamics side of the model has been achieved in the SV algorithm where a fluids model has been obtained which can handle a deformable boundary. What remains is the addition of a real constitutive response at the solid wall boundary via a finite element structural model so that the wall can respond to fluid pressure and the fluid can respond to a physically displaced wall. Time scales of the coupling of the two models into a hybrid model remains a question. Numerical accuracy is also an unknown for this problem.

Projection methods are currently used to solve a variety of problems. The technology of the SV method can be applied to existing projection methods in order to accommodate other deformable domains. It is also of interest to extend the target problem in this thesis to three dimensions. The best way to deal with a three dimensional model would be to employ a Cartesian grid embedded boundary method. The method is based on a finite volume approach to handle irregular cells near boundaries. The time-dependent techniques of the SV method should adapt quite nicely to such an environment.

There are several physical applications for the model of flow in a flexible tube. Hemodynamic flow is an obvious one where the fluid is coupled to a responsive wall. Stenosis in arteries is a problem that could be analyzed, especially in regions behind lumps in vessels where the flow is extremely vortical such that it causes small emboli to break off which clog smaller vessels. Outside of biological applications there are industrial flows like slugging flow in oil pipelines. This problem would require a multiphase flow model.

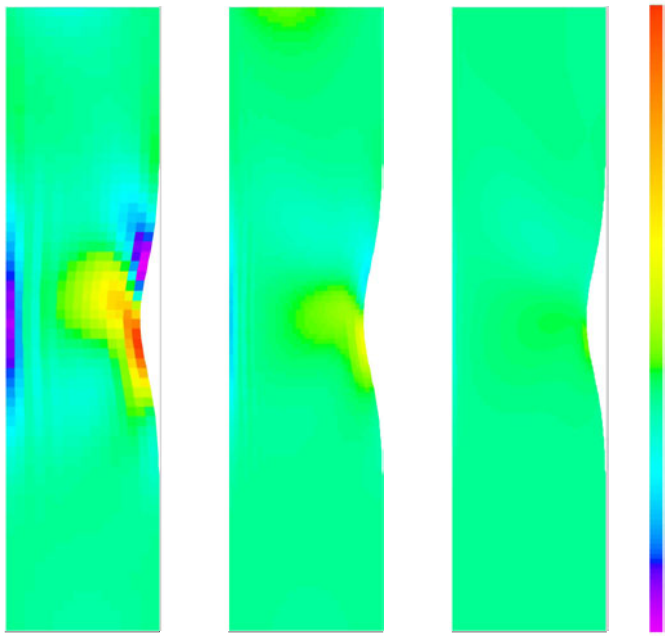

(a)

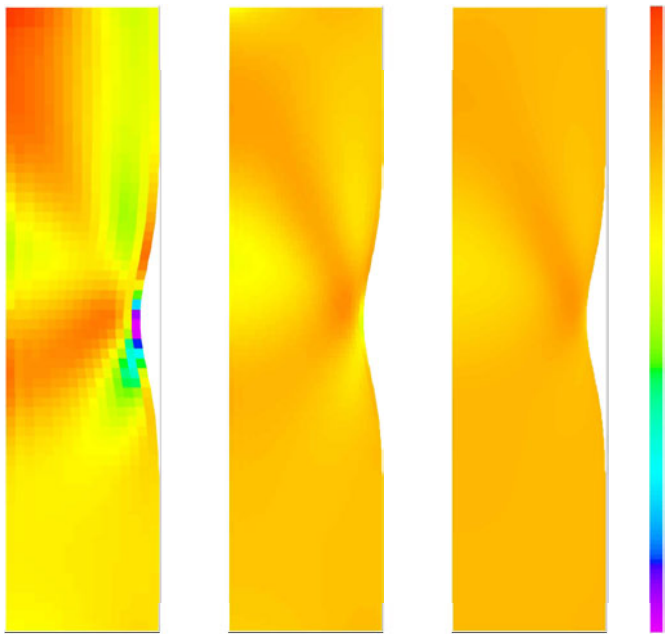

(b)

**Figure 4.2:** Numerical error of SV method for incompressible flow in a flexible tube with inward moving hump at time $t = .5$ (inlet $Re = 8$). (a) $e^{1/16}$, $e^{1/32}$ and $e^{1/64}$ in radial component, $u$ (scale: -.0069 to .0115). (b) $e^{1/16}$, $e^{1/32}$ and $e^{1/64}$ in axial component, $v$ (scale: -.0125 to .0036).

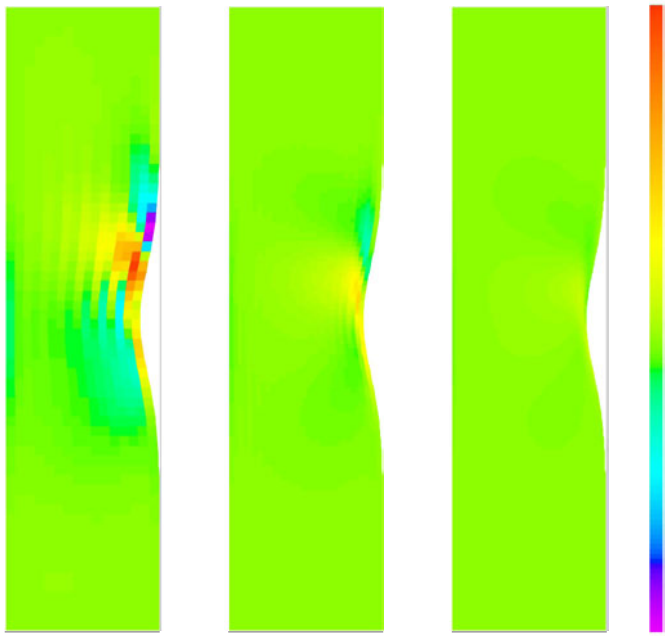

(a)

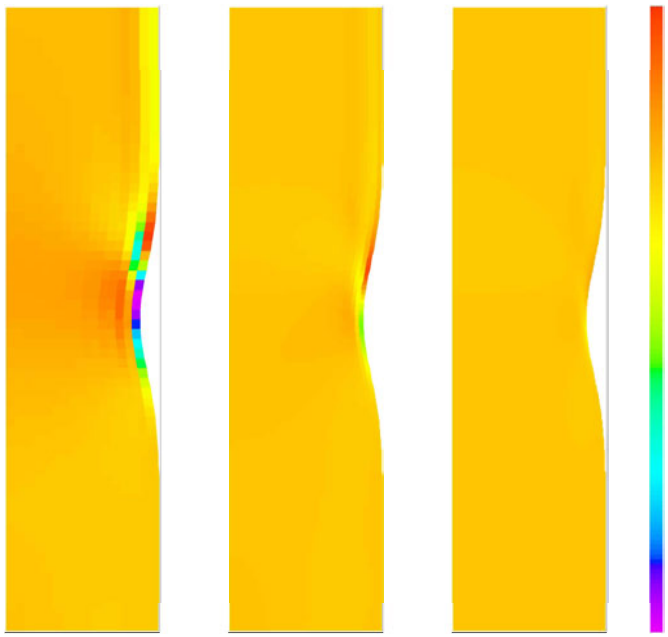

(b)

**Figure 4.3:** Numerical error of SV method for incompressible flow in a flexible tube with inward moving hump at time $t = .5$ (Inlet $Re = 8$). (a) $e^{1/16}$, $e^{1/32}$ and $e^{1/64}$ in radial component, $u$ (scale: -.0305 to .0346). (b) $e^{1/16}$, $e^{1/32}$ and $e^{1/64}$ in axial component, $v$ (scale: -.1191 to .0414).

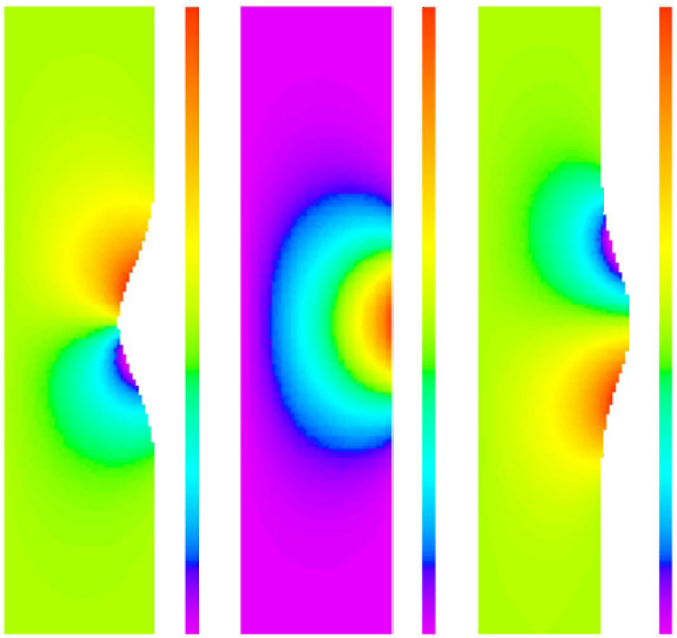

(a)

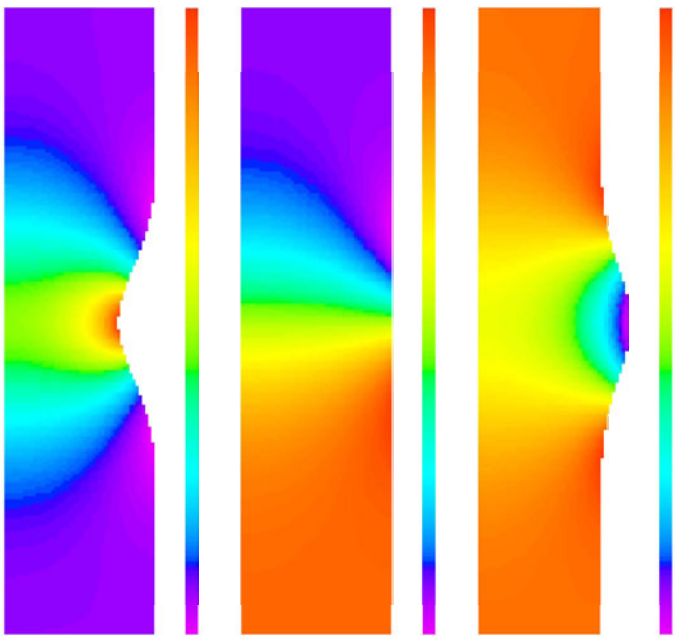

(b)

**Figure 4.4:** Potential velocity for outward moving hump. (a) Plots of radial component of potential velocity at times $t = 0$ (fixed) (scale: -.589 to .589), $t = .5$ (moving) (scale: 0 to .772) and $t = 1$ (fixed) (scale: -.293 to .293). (b) Plots of axial component of potential velocity at times $t = 0$ (fixed) (scale: .909 to 2.207), $t = .5$ (moving) (scale: -.512 to 1.12) and $t = 1$ (fixed) (scale: .428 to 1.05).

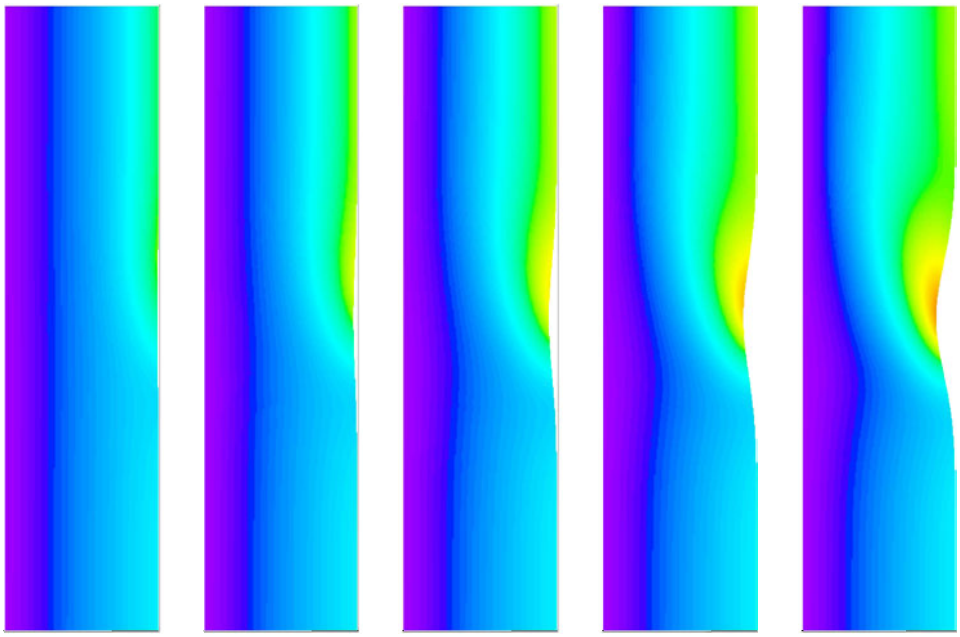

(a)

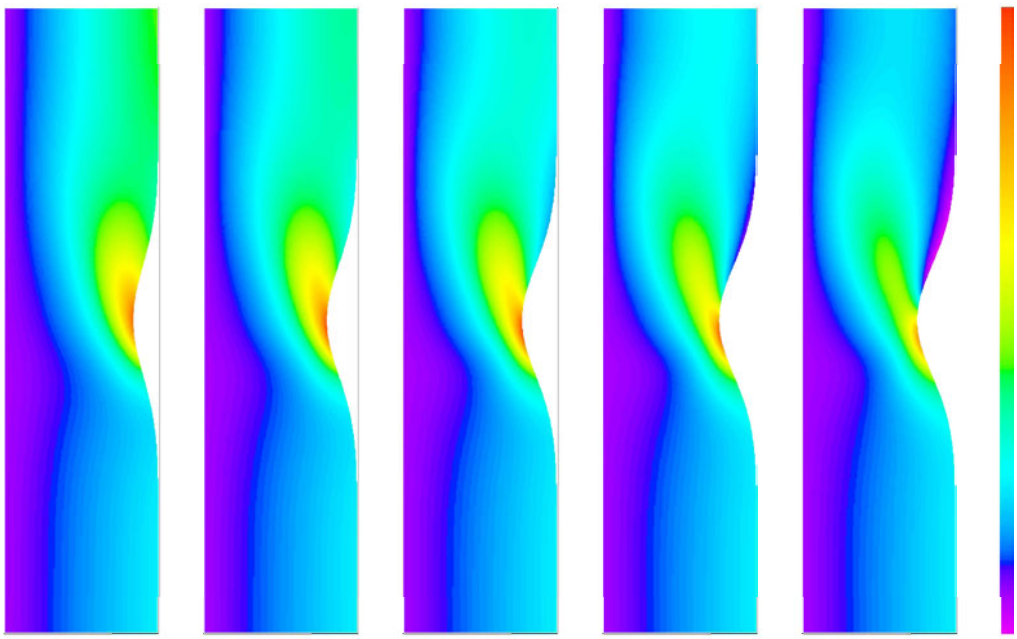

(b)

**Figure 4.5:** Vorticity for incompressible flow in a flexible tube with inward moving hump (inlet $Re = 8$). (a) Times $t = .1, .2, .3, .4, .5$. (b) Times $t = .6, .7, .8, .9, 1$. Note separation and reattachment at $t = .9$ and $t = 1$. (Scale: -1.35 to 21).

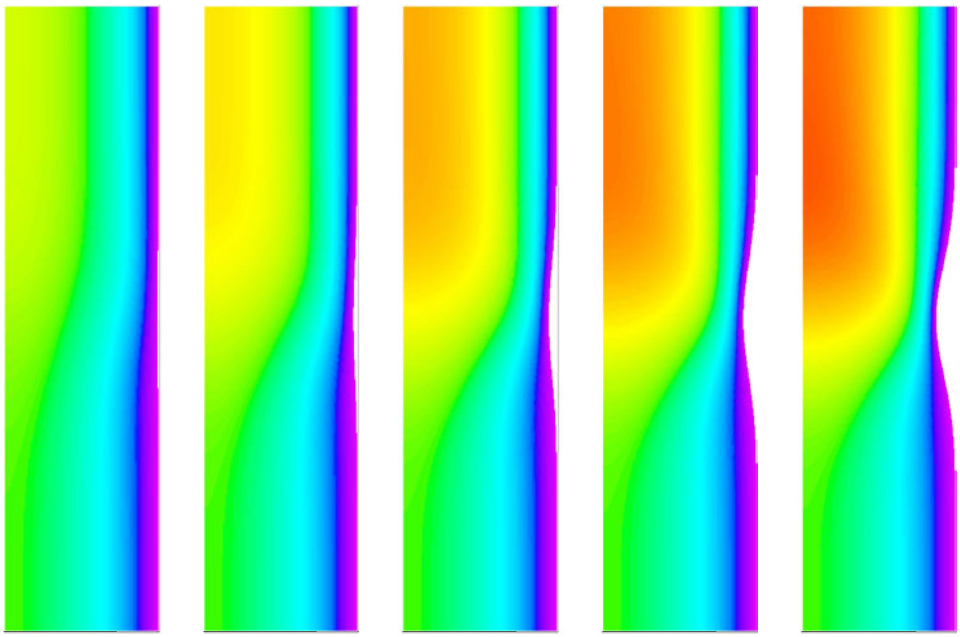

(a)

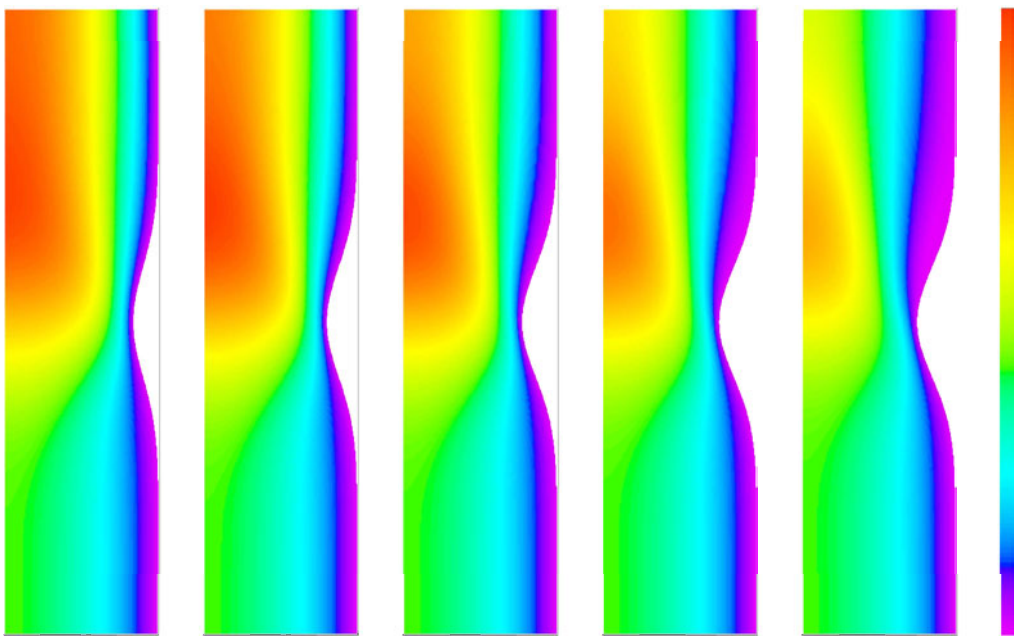

(b)

**Figure 4.6:** Axial velocity for incompressible flow in a flexible tube with inward moving hump (inlet $Re = 8$). (a) Times $t = .1, .2, .3, .4, .5$. (b) Times $t = .6, .7, .8, .9, 1$. (Scale: -.0265 to 4.677).

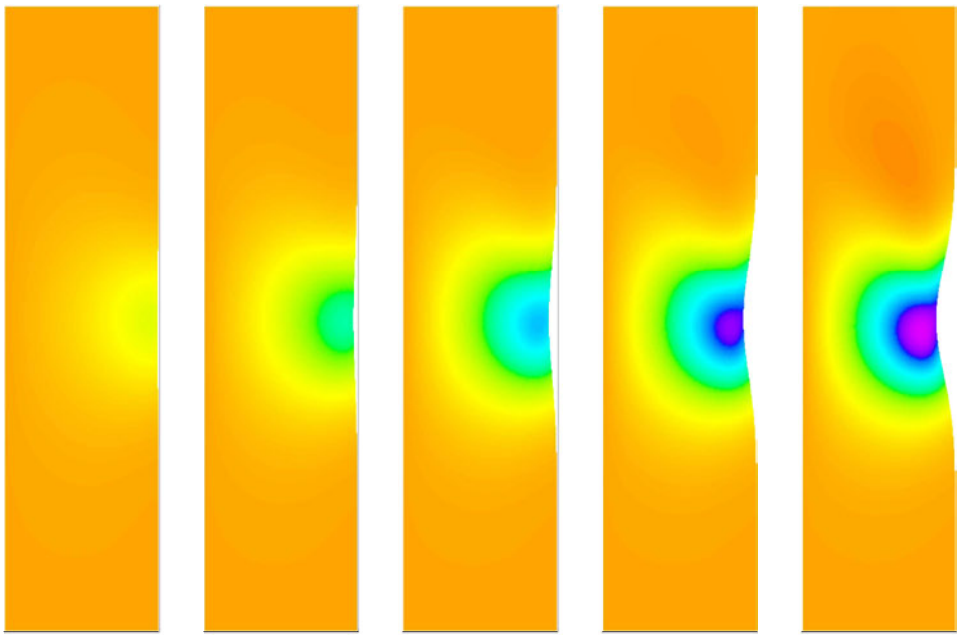

(a)

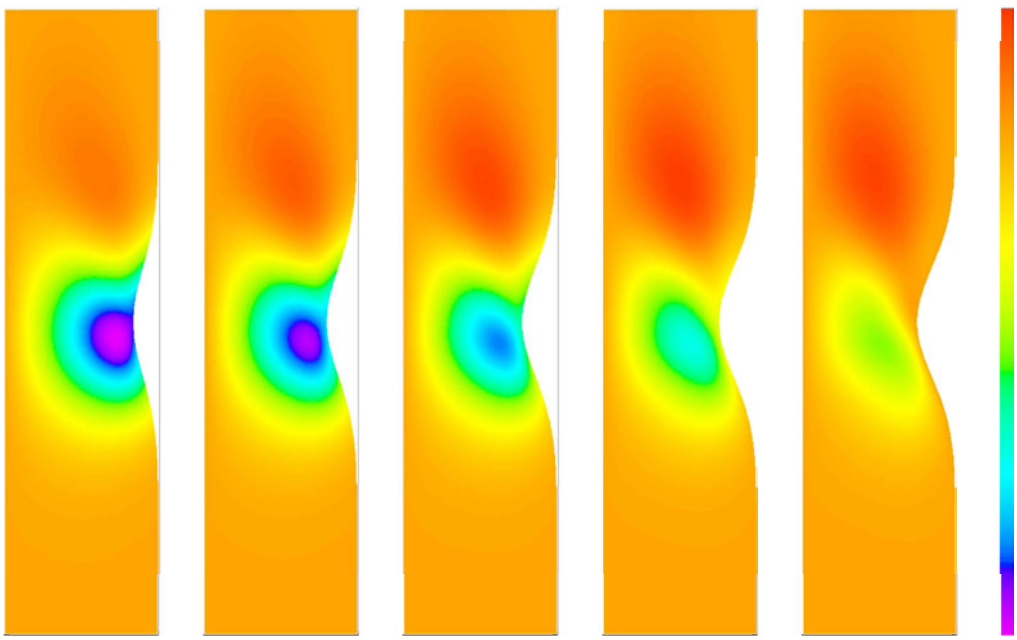

(b)

**Figure 4.7:** Radial velocity for incompressible flow in a flexible tube with inward moving hump (inlet $Re = 8$). (a) Times $t = .1, .2, .3, .4, .5$. (b) Times $t = .6, .7, .8, .9, 1$. (Scale: -.860 to .2092).

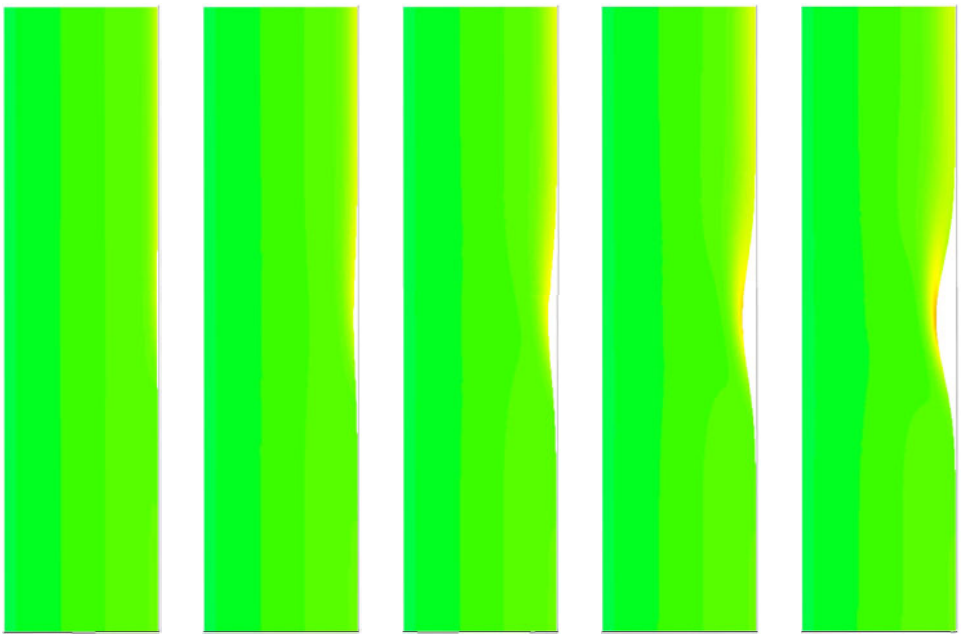

(a)

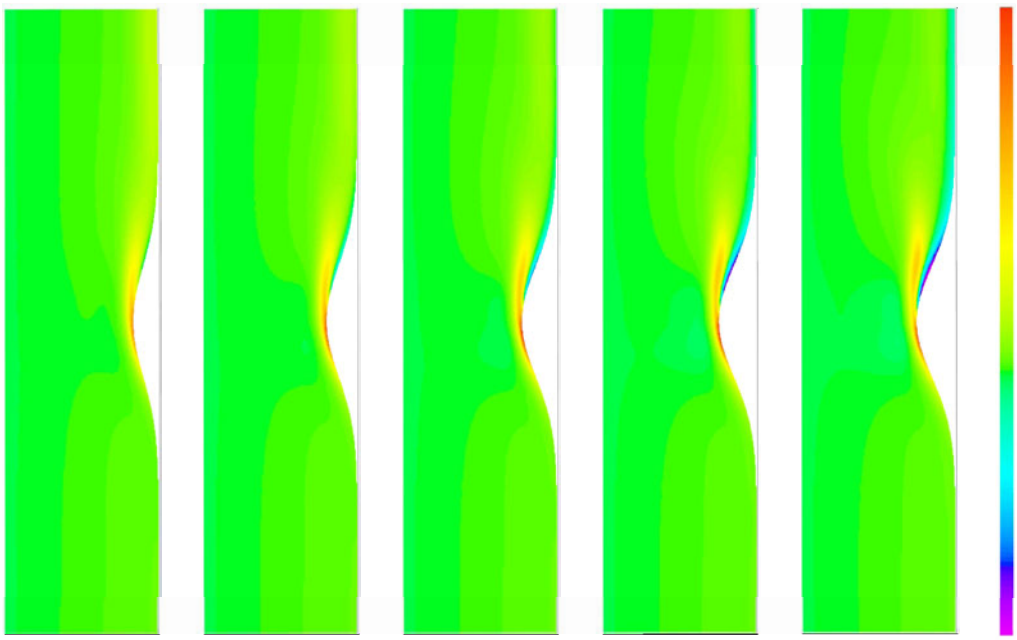

(b)

**Figure 4.8:** Vorticity in tube with inward moving hump (inlet $Re = 200$). (a) Times $t = .1, .2, .3, .4, .5$. (b) Times $t = .6, .7, .8, .9, 1$. Note separation with no reattachment and a recirculation zone curling up at $t = .9$ and $t = 1$. (Scale: -61.11 to 86.05).

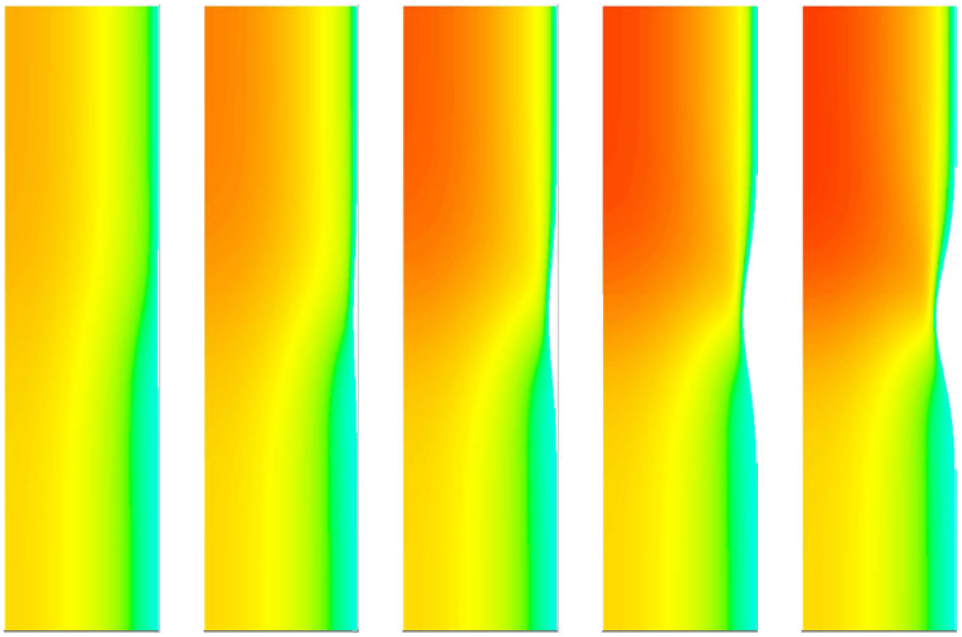

(a)

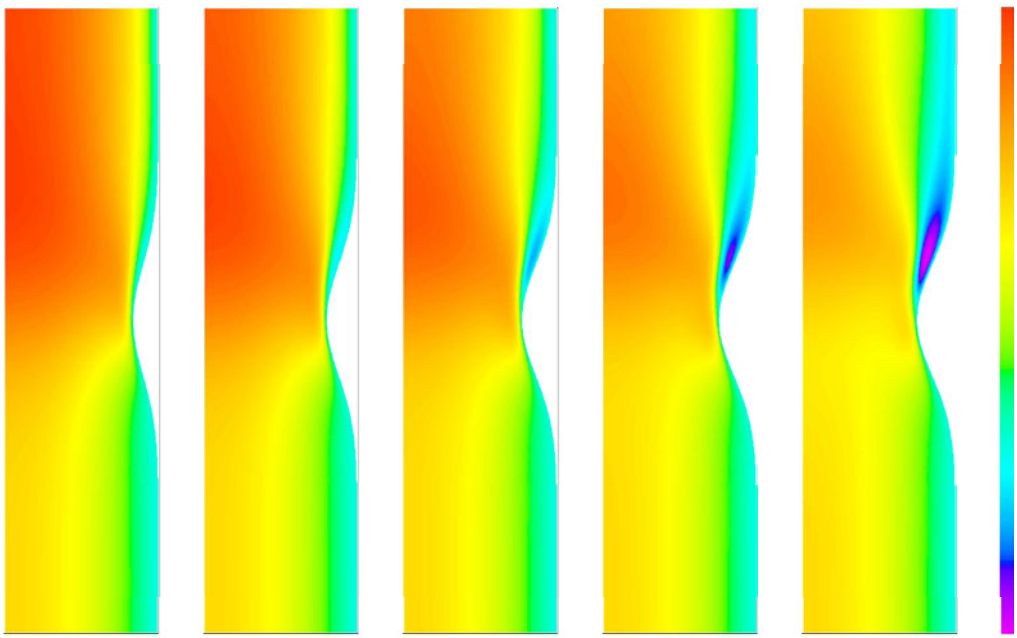

(b)

**Figure 4.9:** Axial velocity in tube with inward moving hump (inlet $Re = 200$). (a) Times $t = .1, .2, .3, .4, .5$. (b) Times $t = .6, .7, .8, .9, 1$. Note recirculation zone curling up at $t = .9$ and $t = 1$. (Scale: -1.41 to 3.466).

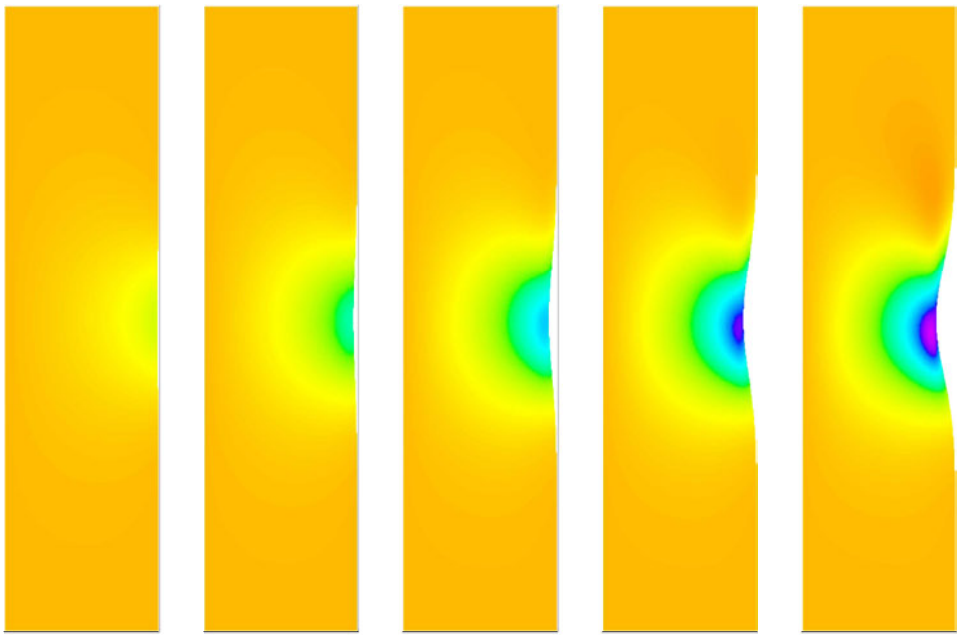

(a)

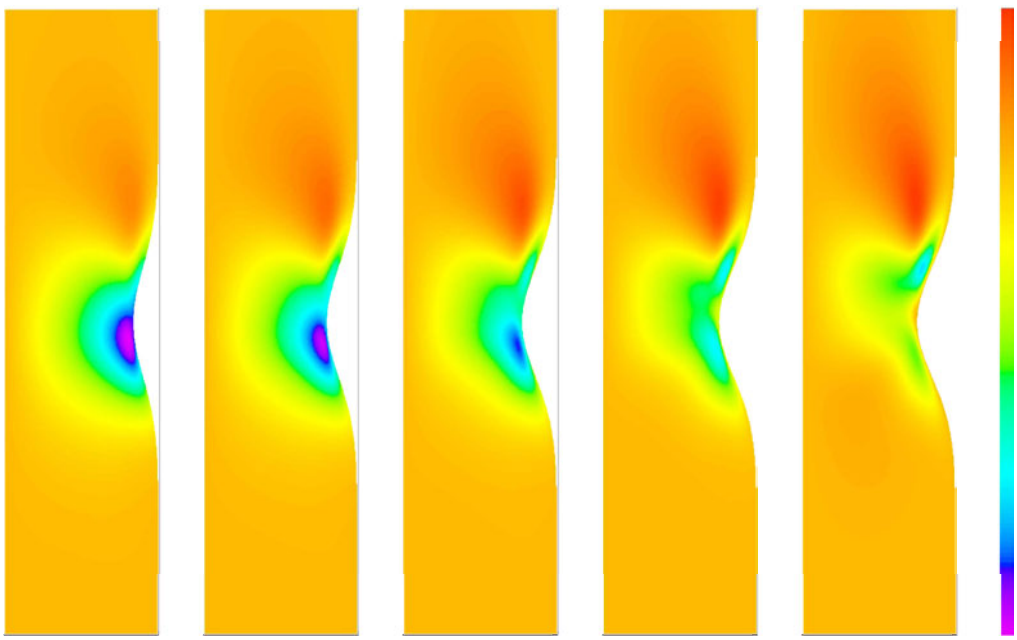

(b)

**Figure 4.10:** Radial velocity in tube with inward moving hump (inlet $Re = 200$). (a) Times $t = .1, .2, .3, .4, .5$. (b) Times $t = .6, .7, .8, .9, 1$. (Scale: -.868 to .265).

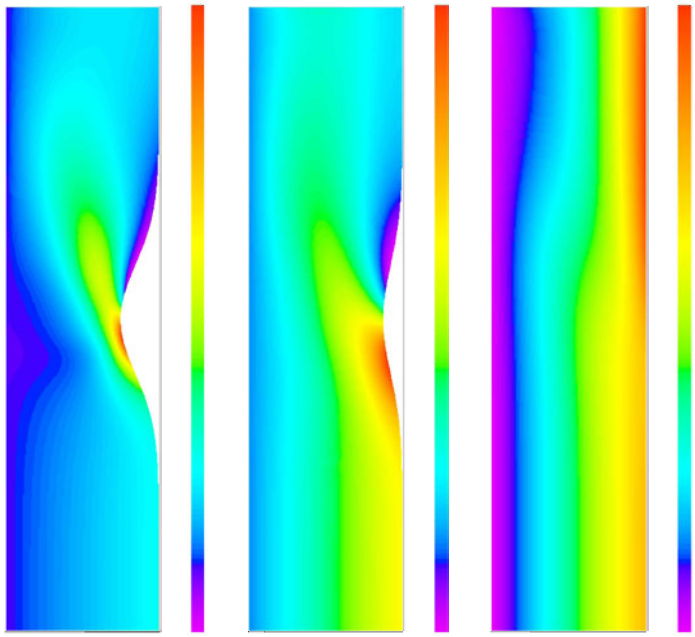

(a)

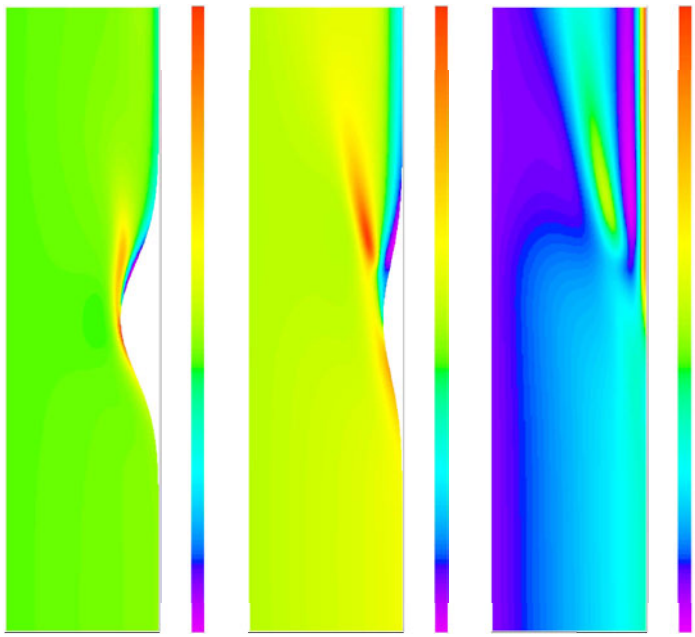

(b)

**Figure 4.11:** Vorticity in expanding tube. (a) Inlet $Re = 16$. Times $t = 1.0$ (scale: -4.44 to 38.91), $t = 1.5$ (scale: -2.34 to 13.45), $t = 2.0$ (scale: .010 to 10.25). (b) Inlet $Re = 400$. Times $t = 1.0$ (scale: -67.41 to 87.15), $t = 1.5$ (scale: -28.65 to 27.52), $t = 2.0$ (scale: -1.56 to 18.73).

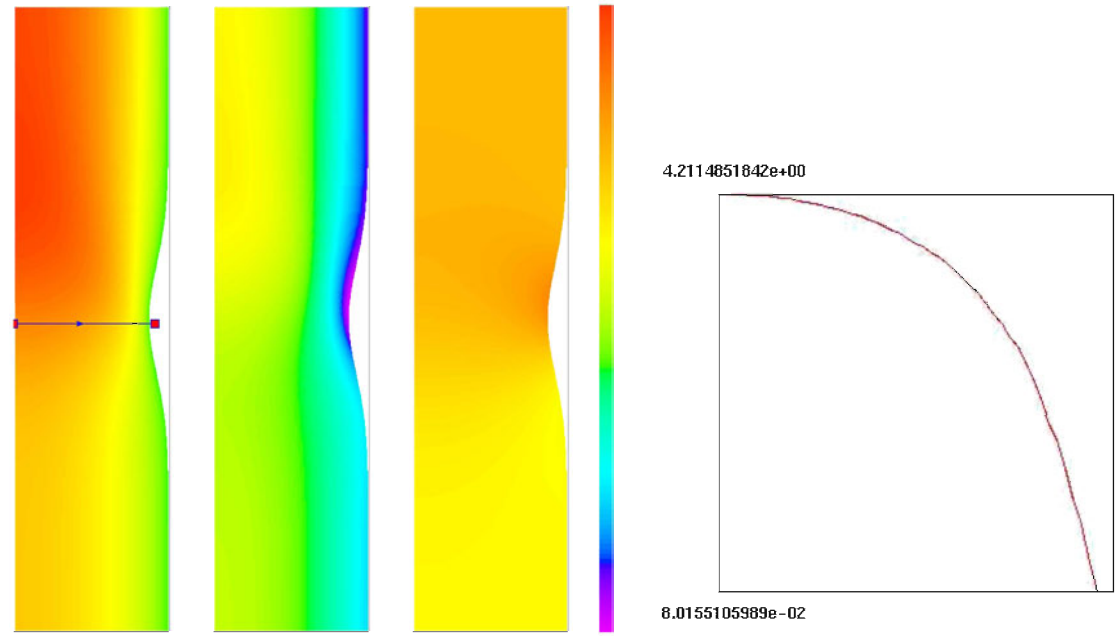


(a)

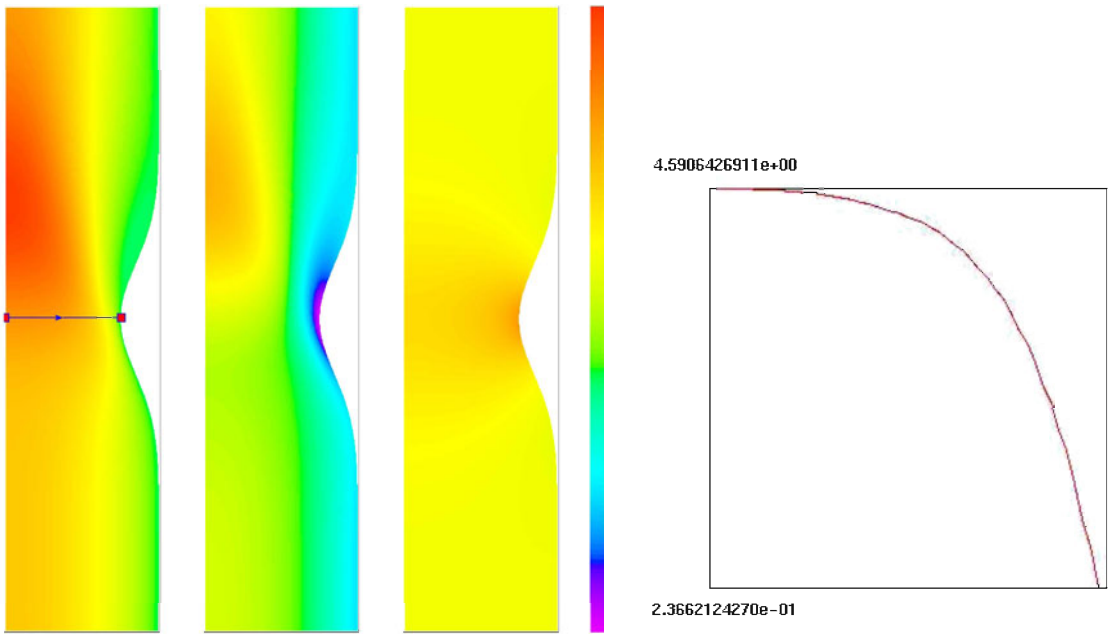


(b)

**Figure 4.12:** Axial velocity in tube with inward moving hump (inlet $Re = 16$). (a) Total axial velocity, vortical axial velocity and potential axial velocity at t=.5 (scale: -4.08 to 5.48) with radial profile of total axial velocity. (b) Total axial velocity, vortical axial velocity and potential axial velocity at t=1.0 (scale: -4.36 to 6.24) with radial profile of total axial velocity. Note vortically driven flow near boundary and potentially driven flow away from boundary.

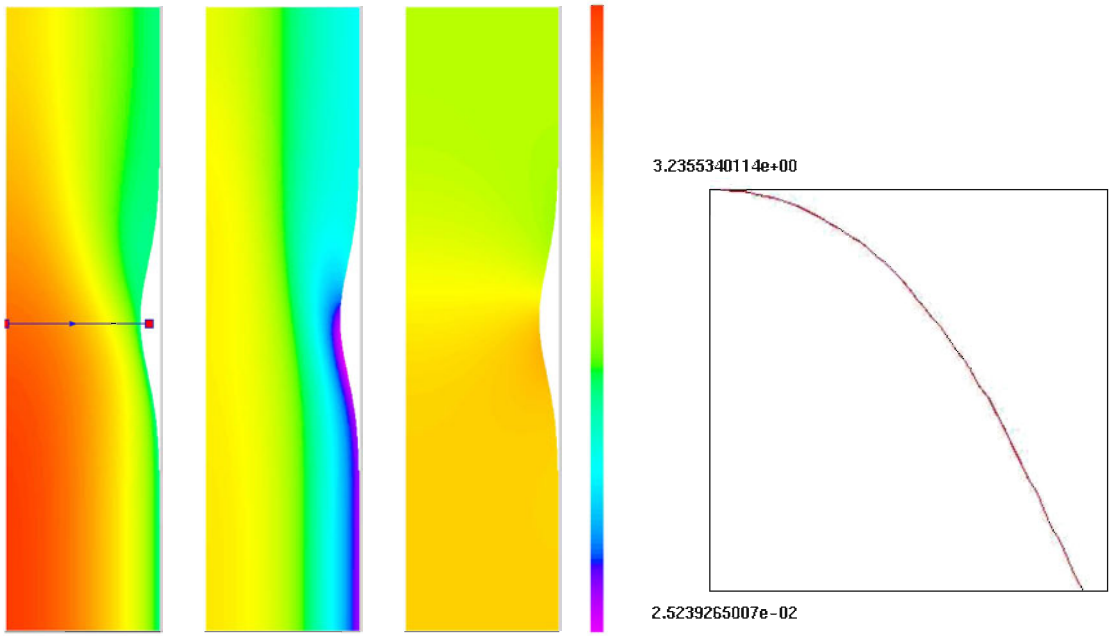


(a)

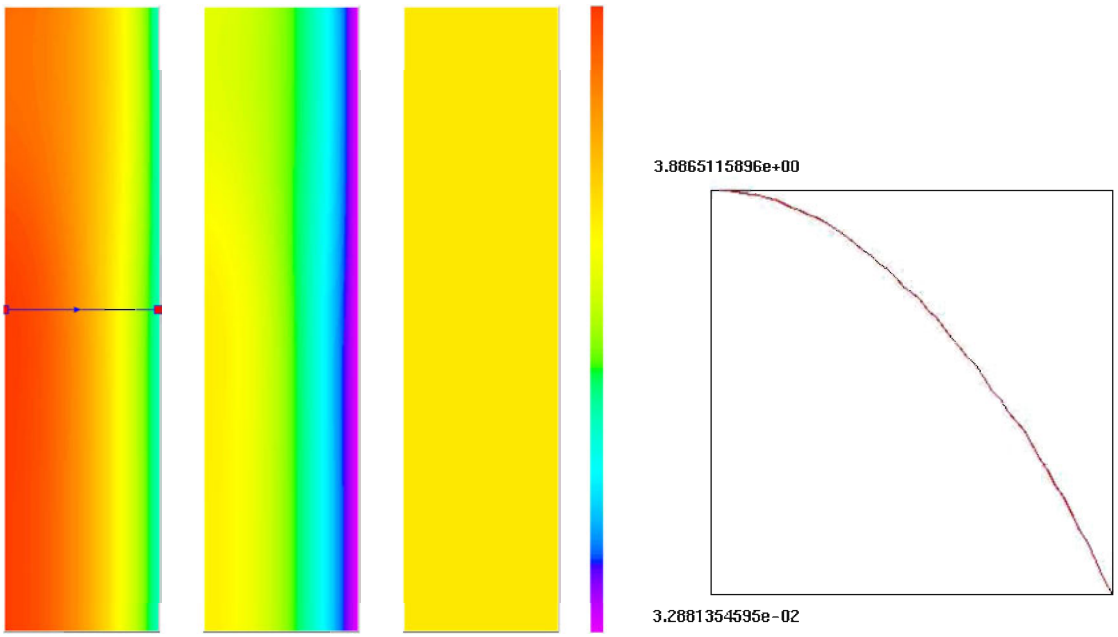


(b)

**Figure 4.13:** Axial velocity in tube with outward moving hump (inlet $Re = 16$). (a) Total axial velocity, vortical axial velocity and potential axial velocity at t=1.5 (scale: -2.36 to 3.72) with radial profile of total axial velocity. (b) Total axial velocity, vortical axial velocity and potential axial velocity at t=2.0 (scale: -1.97 to 3.90) with radial profile of total axial velocity. Note plug flow potential component at $t = 2$ for a boundary at rest.

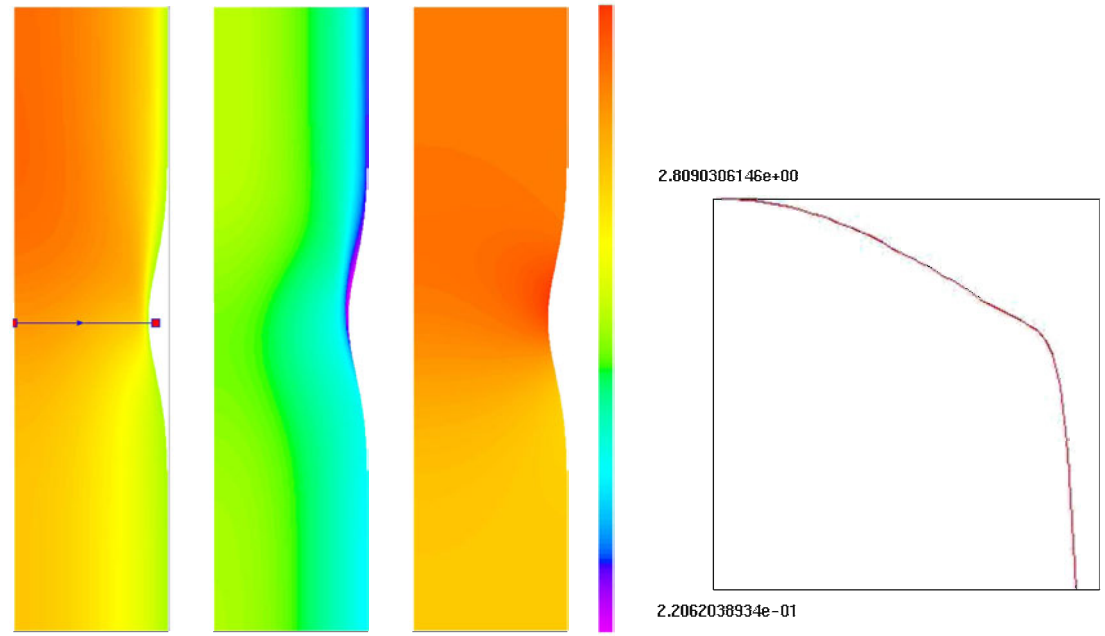


(a)

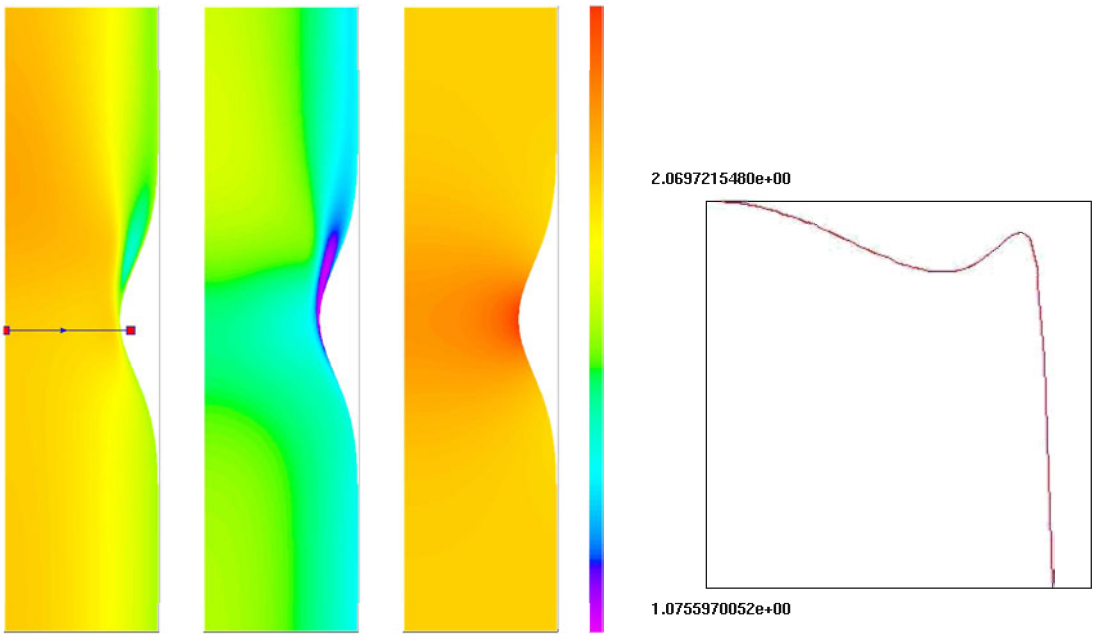


(b)

**Figure 4.14:** Axial velocity in tube with inward moving hump (inlet $Re = 400$). (a) Total axial velocity, vortical axial velocity and potential axial velocity at t=.5 (scale: -4.02 to 4.15) with radial profile of total axial velocity. Note steepness of profile near wall. (b) Total axial velocity, vortical axial velocity and potential axial velocity at t=1.0 (scale: -4.31 to 4.44) with radial profile of total axial velocity. Note "top-hat" profile of an internal laminar jet with void in center of vortical component of flow.

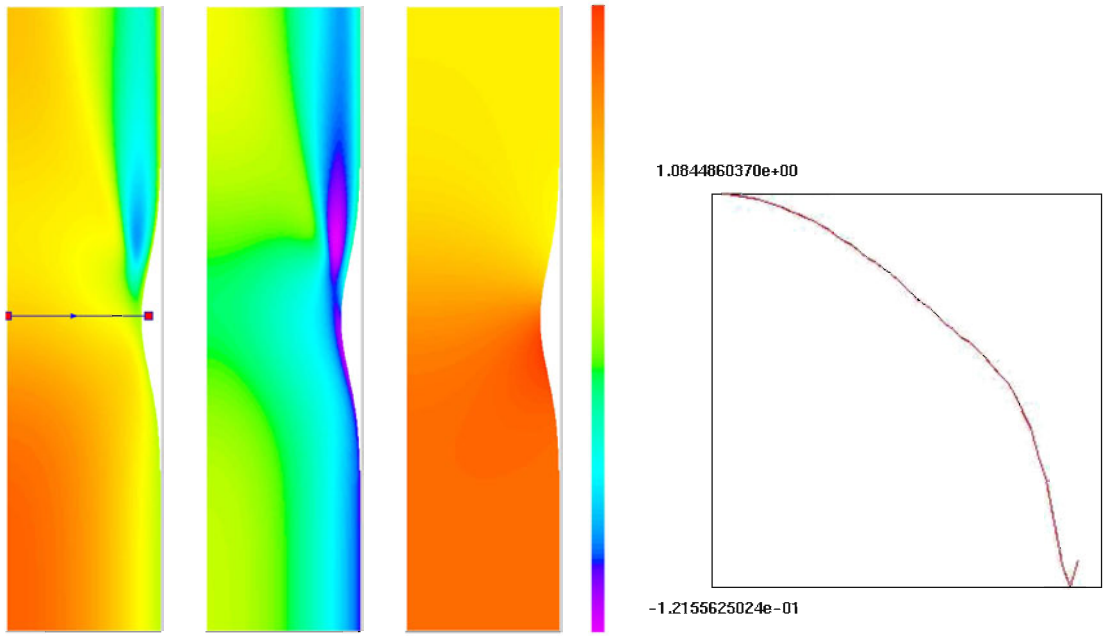


(a)

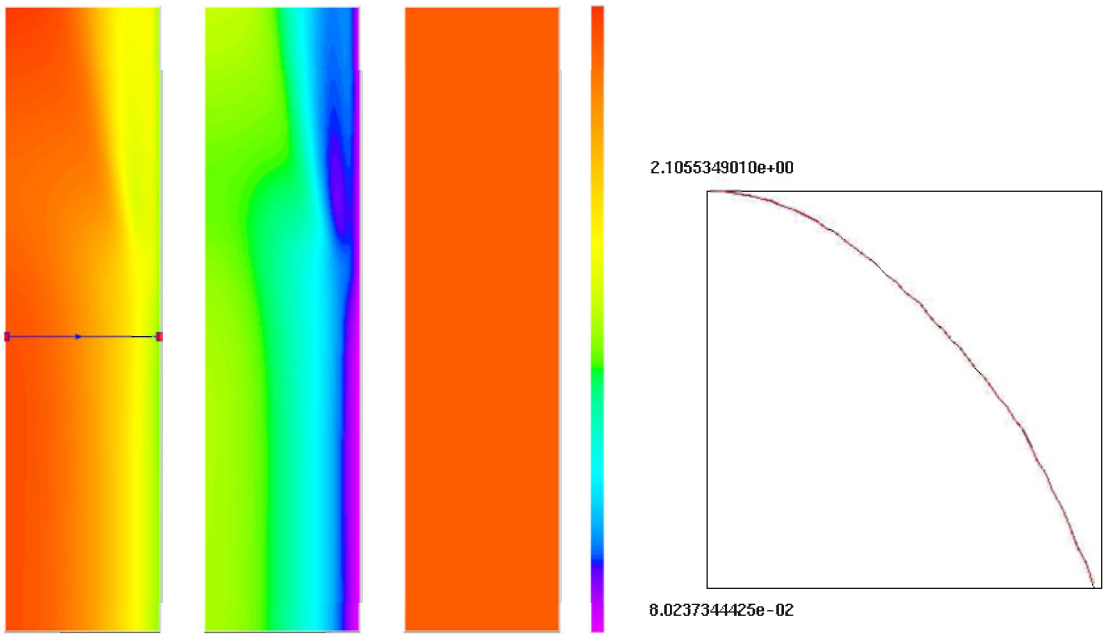


(b)

**Figure 4.15:** Axial velocity in tube with outward moving hump (inlet $Re = 400$). (a) Total axial velocity, vortical axial velocity and potential axial velocity at t=1.5 (scale: -2.50 to 2.40) with radial profile of total axial velocity. (b) Total axial velocity, vortical axial velocity and potential axial velocity at t=2.0 (scale: -1.98 to 2.27) with radial profile of total axial velocity.

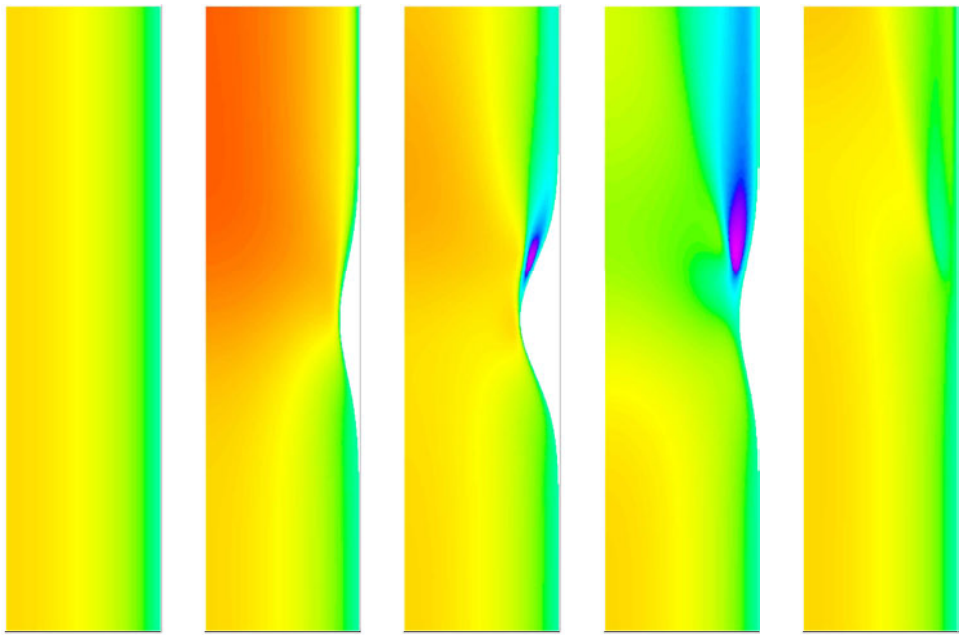

(a)

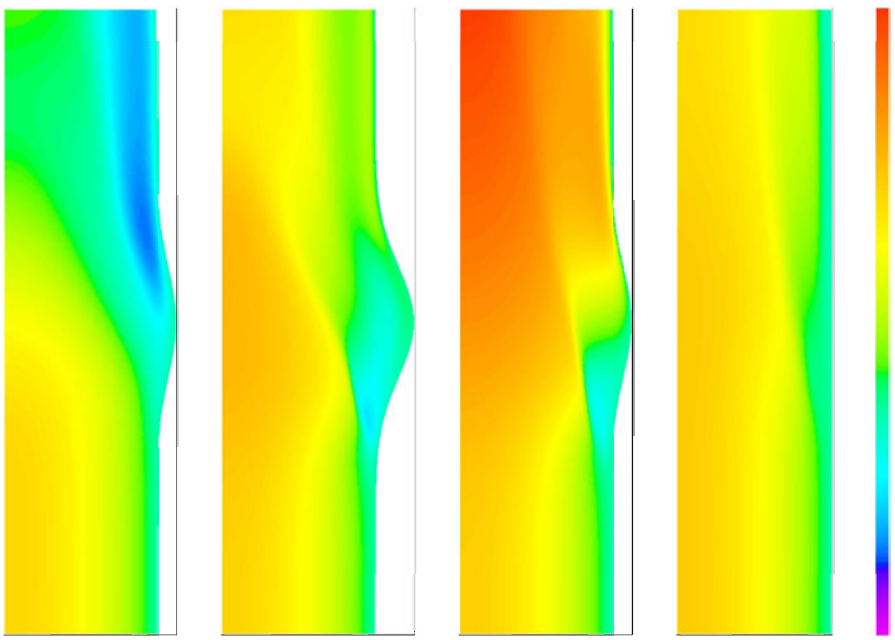

(b)

**Figure 4.16:** Axial velocity in tube with inward/outward moving hump (inlet $Re = 800$). (a) Times $t = 0, .5, 1, 1.5, 2$. (b) Times $t = 2.5, 3, 3.5, 4$. (Scale: -2.113 to 3.781).

# Bibliography

[1] A. Almgren, J. Bell, and W. Szymczak. A numerical method for the incompressible Navier-Stokes equations based on an approximate projection. *SIAM J. Sci. Comput.*, 17:358–369, 1996.

[2] A. S. Almgren, J. B. Bell, P. Colella, and T. Marthaler. A Cartesian grid projection method for the incompressible Euler equations in complex geometries. *SIAM J. Sci. Comput.*, 18(5):1289–1309, 1997.

[3] R. Aris. *Vectors, Tensors, and the Basic Equations of Fluid Mechanics.* Englewood Cliffs, N.J., 1962.

[4] J. B. Bell, P. Colella, and H. M. Glaz. A second-order projection method for the incompressible Navier-Stokes equations. *J. Comput. Phys.*, 85:257–283, 1989.

[5] J. B. Bell, P. Colella, and L. H. Howell. An efficient second-order projection method for viscous incompressible flow. In *Proceedings, AIAA* $10^{th}$ *Computational Fluid Dynamics*, pages 360–367, Honolulu, HI, June 24-26 1991.

[6] J. B. Bell, P. Colella, J. A. Trangenstein, and M. Welcome. Adaptive mesh refinement on moving quadrilateral grids. In *Proceedings, AIAA* $9^{th}$ *Computational Fluid Dynamics Conference*, Buffalo, NY, June 14-16 1989.

[7] J. B. Bell and D. L. Marcus. A 2nd-order projection method for variable-density flows. *J. Comput. Phys.*, 101(2):334–348, 1992.

[8] J. B. Bell, J. Solomon, and W. Szymczak. A second-order projection method for the incompressible Navier-Stokes equations on quadrilateral grids. In *Proceedings, AIAA* $9^{th}$ *Computational Fluid Dynamics Conference*, Buffalo, NY, June 14-16 1989.

[9] T. Belytschko and J. M. Kennedy. Computer models for subassembly simulation. *Nucl. Engrg. Design*, 49:17–38, 1978.

[10] W. Briggs. *A Multigrid Tutorial.* SIAM, Philadelphia, PA, 1987.

[11] A. N. Brooks and T. J. R. Hughes. Streamline upwind/Petrov-Galerkin methods for advection dominated flows. In *Third International Conference on Finite Element Methods in Fluid Flows*, Banff, Canada, 1980.

[12] A. J. Chorin. A numerical method for solving incompressible viscous flow problems. *J. Comput. Phys.*, 2:12–26, 1967.

[13] A. J. Chorin. Numerical solutions of the Navier-Stokes equations. *Math. Comp.*, 22:745–762, 1968.

[14] A. J. Chorin. On the convergence of discrete approximations to the Navier-Stokes equations. *Math. Comp.*, 23:341–353, 1969.

[15] A. J. Chorin. Numerical study of slightly viscous flow. *J. Fluid Mech.*, 57:785–796, 1973.

[16] A. J. Chorin. Vortex methods and boundary instability. *SIAM J. Sci. Stat. Comput.*, 3:1–21, 1980.

[17] P. Colella. Multidimensional upwind methods for hyperbolic conservation laws. *J. Comput. Phys.*, 87:171–200, 1990.

[18] P. Colella and K. Pao. An all speed algorithm. *J. Comput. Phys.*, 1997.

[19] R. Cortez. An impulse-based approximation of fluid motion due to boundary forces. *J. Comput. Phys.*, 123:341–353, 1996.

[20] J. Donea. *Computational Methods for Transient Analysis*, chapter 10. Elsevier Science Publishers B.V., 1983.

[21] J. Donea. A Taylor-Galerkin method for convective transport problems. *Int. J. Numer. Meth. Engrg.*, 20:101–119, 1984.

[22] J. Donea. Generalized Galerkin methods for convection dominated transport phenomena. *Appl. Mech. Rev.*, 44(5):205–214, 1991.

[23] J. Donea, P. Fasoli-Stella, and S. Giuliani. Lagrangian and Eulerian finite element techniques for transient fluid-structure interaction problems. In *Transactions, 4th SMIRT Conference*, San Francisco, August 15-19 1977.

[24] J. Donea and L. Quartapelle. An introduction to finite element methods for transient advection problems. *Comp. Meth. Appl. Mech. Engrg.*, 95:169–203, 1992.

[25] V. C. Dotti. On second-order accurate integrators in discrete elasto-plasticity. Master's thesis, University of California, Berkeley, 1995.

[26] L. P. Franca and S. L. Frey. Stabilized finite element methods. II. The incompressible Navier-Stokes equations. *Comp. Meth. Appl. Mech. Engrg.*, 99(2-3):209–233, 1992.

[27] L. P. Franca, S. L. Frey, and T. J. R. Hughes. Stabilized finite element methods. I. Application to the advective-diffusive model. *Comp. Meth. Appl. Mech. Engrg.*, 95:253–276, 1992.

[28] Y. C. Fung. *Foundations of Solid Mechanics.* Prentice-Hall, 1965.

[29] F. H. Harlow. Numerical methods for fluid dynamics. Technical report, Los Alamos Scientific Laboratory, 1969.

[30] J. C. Heinrich and O. C. Zienkiewicz. The finite element method and "upwinding" techniques in the numerical solution of convection dominated flow problems. In T. J. R. Hughes, editor, *Finite Element Methods for Convection Dominated Flows*, New York, 1979. ASME.

[31] J. A. Hilditch. *A projection method for low Mach number reacting flow in the fast chemistry limit.* PhD thesis, University of California, Berkeley, 1997.

[32] C. W. Hirt, A. A. Amsden, and J. L. Cook. An arbitrary Lagrangian-Eulerian computing method for all speed flows. *J. Comput. Phys.*, 14:227, 1974.

[33] C. W. Hirt and B. D. Nichols. Volume of fluid (VOF) method for the dynamics of free boundaries. *J. Comput. Phys.*, 39(1):201–225, 1981.

[34] T. J. R. Hughes, L. P. Franca, and G. M. Hulbert. A new finite element method for computational fluid dynamics: VII. The Galerkin/least-squares method for advective-diffusive equations. *Comp. Meth. Appl. Mech. Engrg.*, 73:173–189, 1989.

[35] T. J. R. Hughes, W. K. Liu, and T. K. Zimmerman. Lagrangian-Eulerian finite element formulation for incompressible viscous flows. In *U.S.-Japan Seminar on Interdisciplinary Finite Element Analysis*, Cornell University, Ithaca, NY, August 7-11 1978.

[36] H. S. Johansen. *Cartesian grid embedded boundary finite difference methods for elliptic and parabolic partial differential equations on irregular domains.* PhD thesis, University of California, Berkeley, 1997.

[37] H. S. Johansen and P. Colella. An approximate projection method for the variable density Navier-Stokes equations on mapped grids. Unpublished.

[38] C. Johnson. *Numerical Solution of Partial Differential Equations by the Finite Element Method.* Studentliteratur, Sweden, 1987.

[39] M. Lai. *A projection method for reacting flow in the zero Mach number limit.* PhD thesis, University of California, Berkeley, 1994.

[40] R. J. LeVeque. Immersed interface methods for Stokes flow with elastic boundaries or surface tension. *SIAM J. Sci. Comput.*, 18(3):709–735, 1997.

[41] D. Liepmann. Private conversation, 1998.

[42] H. W. Liepmann and J. Laufer. Investigation of free turbulent mixing. *NACA Tech. Note*, 1258, 1947.

[43] L. E. Malvern. *Introduction to the Mechanics of a Continuous Medium.* Prentice-Hall, 1969.

[44] A. Masud and T. J. R. Hughes. A space-time Galerkin/least-squares finite element formulation of the Navier-Stokes equations for moving domain problems. *Comp. Meth. Appl. Mech. Engrg.*, 146:91–126, 1997.

[45] M. L. Minion. On the stability of Godunov-projection methods for incompressible flow. *J. Comput. Phys.*, 123(2):435–449, 1996.

[46] K. W. Morton. Finite difference and finite element methods. *Comput. Phys. Communic.*, 12:99–108, 1976.

[47] K. W. Morton. Generalized Galerkin methods for hyperbolic problems. *Comp. Meth. Appl. Mech. Engrg.*, 52:847–871, 1985.

[48] K. W. Morton and A. K. Parrott. Generalized Galerkin methods for first-order hyperbolic equations. *J. Comput. Phys.*, 36:249–270, 1980.

[49] P. M. Naghdi. ME 185, Continuum mechanics class notes, Department of Mechanical Engineering, University of California, Berkeley.

[50] W. F. Noh. *Methods in Computational Physics*, volume 3, page 117. Academic Press, New York, 1964.

[51] C. S. Peskin. Flow patterns around heart valves: A numerical method. *J. Comput. Phys.*, 10:252–271, 1972.

[52] C. S. Peskin and D. M. McQueen. Cardiac fluid dynamics. *Crit. Rev. Biomed. Engrg.*, 20(5-6):451–459, 1992.

[53] L. Petzold. Differential/algebraic equations are not ODE's. *SIAM J. Sci. Stat. Comput.*, 3(3):367–384, 1982.

[54] R. Peyret and T. D. Taylor. *Computational Methods for Fluid Flow.* Springer-Verlag, 1983.

[55] K. Sawada and S. Takanashi. A numerical investigation on wing/nacelle interferences of USB configuration. In *Proceedings, AIAA* $25^{th}$ *Aerospace Sciences Meeting*, Reno, NV, 1987. AIAA paper 87-0455.

[56] J. C. Simo and S. Govindjee. Nonlinear B-stability and symmetry preserving return mapping algorithms for plasticity and viscoplasticity. *Int. J. Numer. Meth. Engrg.*, 31:151–176, 1991.

[57] G. A. Sod. A compressible vortex method with application to the interaction of an oblique shock wave with a boundary layer. *Appl. Numer. Math.*, 8:257–273, 1991.

[58] J. G. Trulio. Technical Report AFWL-Tr-66-19, Air Force Weapons Laboratory, June 1966.

[59] N. P. Weatherill and C. A. Forsey. Grid generation and flow calculations for aircraft geometries. *J. Aircraft*, 22:855–860, 1985.